

Seeing in the dark – II. Cosmic shear in the Sloan Digital Sky Survey

Eric M. Huff,^{1★} Tim Eifler,² Christopher M. Hirata,³ Rachel Mandelbaum,^{4,5}
David Schlegel⁶ and Uroš Seljak^{6,7,8,9}

¹Department of Astronomy, University of California at Berkeley, Berkeley, CA 94720, USA

²Center for Cosmology and Astro-Particle Physics, The Ohio State University, 191 W. Woodruff Avenue, Columbus, OH 43210, USA

³Department of Astronomy, Caltech M/C 350-17, Pasadena, CA 91125, USA

⁴Department of Astrophysical Sciences, Princeton University, Peyton Hall, Princeton, NJ 08544, USA

⁵Department of Physics, Carnegie Mellon University, Pittsburgh, PA 15213, USA

⁶Lawrence Berkeley National Laboratory, Berkeley, CA 94720, USA

⁷Space Sciences Lab, Department of Physics and Department of Astronomy, University of California, Berkeley, CA 94720, USA

⁸Institute of the Early Universe, Ewha Womans University, Seoul, Korea

⁹Institute for Theoretical Physics, University of Zurich, CH-8006 Zurich, Switzerland

Accepted 2014 January 17. Received 2014 January 16; in original form 2011 December 15

ABSTRACT

Statistical weak lensing by large-scale structure – cosmic shear – is a promising cosmological tool, which has motivated the design of several large upcoming surveys. Here, we present a measurement of cosmic shear using co-added Sloan Digital Sky Survey (SDSS) imaging in 168 square degrees of the equatorial region, with $r < 23.5$ and $i < 22.5$, a source number density of 2.2 per arcmin² and mean redshift of $z_{\text{med}} = 0.52$. These co-adds were generated using a new method described in the companion [Paper I](#) that was intended to minimize systematic errors in the lensing measurement due to coherent point spread function anisotropies that are otherwise prevalent in the SDSS imaging data. We present measurements of cosmic shear out to angular separations of 2°, along with systematics tests that (combined with those from [Paper I](#) on the catalogue generation) demonstrate that our results are dominated by statistical rather than systematic errors. Assuming a cosmological model corresponding to *Wilkinson Microwave Anisotropy Probe 7* (*WMAP7*) and allowing only the amplitude of matter fluctuations σ_8 to vary, we find a best-fitting value of $\sigma_8 = 0.636^{+0.109}_{-0.154}$ (1σ); without systematic errors this would be $\sigma_8 = 0.636^{+0.099}_{-0.137}$ (1σ). Assuming a flat Λ cold dark matter model, the combined constraints with *WMAP7* are $\sigma_8 = 0.784^{+0.028}_{-0.026}$ (1σ) $^{+0.055}_{-0.054}$ (2σ) and $\Omega_m h^2 = 0.1303^{+0.0047}_{-0.0048}$ (1σ) $^{+0.009}_{-0.009}$ (2σ); the 2σ error ranges are, respectively, 14 and 17 per cent smaller than *WMAP7* alone.

Key words: gravitational lensing: weak – surveys – cosmology: observations.

1 INTRODUCTION

As a result of gravitational lensing, large-scale inhomogeneities in the matter density field produce small but systematic fluctuations in the sizes, shapes, and fluxes of distant objects that are coherent across large scales. This effect was first suggested as a tool for constraining the form of the metric in 1966 by Kristian & Sachs (1966). In a more modern context, the two-point statistics of lensing fluctuations allow the only truly direct measurement of the matter power spectrum and the growth of structure at late times, when dark energy has caused an accelerated expansion of the Universe (Riess et al. 1998; Perlmutter et al. 1999) and affected the growth of structure. Many studies have pointed out that high signal-to-noise ratio cosmic shear measurements would be extraordinarily sensitive

probes of cosmological parameters (e.g. Huterer 1998; Benabed & van Waerbeke 2004), which led to it being flagged as one of the most promising probes of dark energy by the Dark Energy Task Force (Albrecht et al. 2006). Direct measurements of the growth of structure also offer the opportunity to test alternative models of gravity (e.g. Laszlo et al. 2011).

Cosmic shear measurements were attempted as early as 1967 (Kristian 1967), but until the turn of the millennium (Bacon, Refregier & Ellis 2000; Kaiser, Wilson & Luppino 2000; van Waerbeke et al. 2000; Wittman et al. 2000), no astronomical survey had the statistical power to detect it. The difficulty of the measurement is a consequence of the near homogeneity and isotropy of the universe. An order-unity distortion to galaxy images requires an integrated line-of-sight matter overdensity of

$$\Sigma_{\text{crit}} = \frac{c^2}{4\pi G} \frac{d_s}{d_L d_{LS}}, \quad (1)$$

★E-mail: huff.791@osu.edu

where d_s , d_L , and d_{LS} are the angular diameter distances from the observer to the background source, from the observer to the lens, and from the lens to the background source, respectively. A fluctuation in the surface density $\Delta\Sigma$ leads to a shear distortion $\gamma \sim \Delta\Sigma/\Sigma_{\text{crit}}$.

Averaged over large (~ 100 Mpc) scales, typical line-of-sight matter fluctuations are only $10^{-3}\Sigma_{\text{crit}}$. The primary source of noise in the shear measurement, the random intrinsic dispersion in galaxy shapes, is orders of magnitude larger; typically the shape noise results in a dispersion in the shear of $\sigma_\gamma = 0.2$. Worse, even in modern ground-based astronomical imaging surveys, the coherent distortions – or point spread function (PSF) – induced by effects of the atmosphere, telescope optics, and detectors are typically several times larger than the cosmological signal (e.g. Heymans et al. 2011; Huff et al. 2011, hereafter Paper I). Estimating the distances to the background sources is both crucial (Ma, Hu & Huterer 2006) and difficult (Ma & Bernstein 2008; Bernstein & Huterer 2010); errors there will modulate the amplitude of the signal through Σ_{crit} , biasing inference of the growth of structure.

These obstacles define the observational problem. While the existence of cosmic shear has been established by the first studies to detect the effect, the full potential of cosmological lensing remains to be exploited. Few data sets capable of achieving the signal strength for a cosmologically competitive measurement presently exist – the Canada–France–Hawaii Telescope Legacy Survey (Hoekstra et al. 2006; Semboloni et al. 2006; Benjamin et al. 2007; Fu et al. 2008), the Cosmological Evolution Survey (COSMOS; Massey et al. 2007a; Schrabback et al. 2010), and the subset of the SDSS imaging studied here. However, several large surveys are planned for the immediate and longer term future that will substantially expand the amount of available data for cosmological weak lensing studies. In the next few years, these include Hyper Suprime-Cam (HSC; Miyazaki et al. 2006), Dark Energy Survey (DES;¹ The Dark Energy Survey Collaboration 2005), the Kiilo-Degree Survey,² and the Panoramic Survey Telescope and Rapid Response System (Pan-STARRS,³ Kaiser et al. 2010). Further in the future, there are even more ambitious programmes such as the Large Synoptic Survey Telescope (LSST;⁴ LSST Science Collaboration 2009), *Euclid*,⁵ and the Wide-Field Infrared Survey Telescope.⁶

For this work, we have combined several methods discussed in the literature as viable techniques for measuring cosmic shear while removing common systematic errors. In Paper I, we began with the PSF model generated by the Sloan Digital Sky Survey (SDSS) pipeline over ~ 250 deg² that had been imaged many times, and employed a rounding kernel method similar to that proposed in Bernstein & Jarvis (2002). The result, after appropriate masking of problematic regions, was 168 square degrees of deep co-added imaging with a well controlled, homogeneous PSF and sufficient galaxy surface density to measure a cosmic shear signal. The usable area in r band was only 140 square degrees because of a PSF model error problem on the camcol 2 charge-coupled device (CCD), which is suspected to be an amplifier non-linearity problem.

In this work, we use the catalogue from Paper I to produce a cosmic shear measurement that is dominated by statistical errors. Section 3 enumerates the primary sources of systematic error when

measuring cosmic shear using our catalogue (the properties of which are summarized briefly in Section 2), and describes our approaches to constraining each of them. In Section 4, we outline our correlation function estimator and several transformations of it that are used for systematics tests. Our methods for estimating covariance matrices for our observable quantities (both due to statistical and systematic errors) are described in Section 5. Finally, Section 6 presents the constraining power of this measurement alone for a fiducial cosmology, and in combination with the 7-year *Wilkinson Microwave Anisotropy Probe* (WMAP7; Komatsu et al. 2011) parameter constraints to produce a posterior probability distribution over $\Omega_m h^2$, $\Omega_b h^2$, σ_8 , n_s , and w . We show that in addition to its value as an independent measurement of the late-time matter power spectrum, this measurement provides some additional constraining power over WMAP7 within the context of Λ cold dark matter (Λ CDM). We conclude with some lessons for the future in Section 7.

While this work was underway, we learned of a parallel effort by Lin et al. (2012). These two efforts use different methods of co-addition, different shape measurement codes, different sets of cuts for the selection of input images and galaxies, and analyse their final results in different ways; what they have in common is their use of SDSS data (not necessarily the same sets of input imaging) and their use of the SDSS PHOTO pipeline for the initial reduction of the single-epoch data and the final reduction of the co-added data (however, they use different versions of PHOTO). Using these different methods, both groups have extracted the cosmic shear signal and its cosmological interpretations. We have coordinated submission with them but have not consulted their results prior to this, so these two analysis efforts are independent, representing versions of two independent pipelines.

2 CATALOGUES

Paper I describes a co-add imaging data set, optimized for cosmic shear measurement, constructed from single-epoch SDSS images in the Stripe 82 equatorial region, with right ascension (RA) $-50^\circ < \text{RA} < +45^\circ$ and declination $-1^\circ 25' < \text{Dec.} < +1^\circ 25'$. In that work, we apply an adaptive rounding kernel to the single-epoch images to null the effects of PSF anisotropy and match to a single homogeneous PSF model for the entire region, and show that in the resulting shear catalogues, the amplitude of the galaxy shape correlations due to PSF anisotropy at angular separations greater than 1 arcmin is negligible compared to the expected cosmic shear statistical errors.

The final shape catalogue described in that work consists of 1067 031 r -band and 1251 285 i -band shape measurements with characteristic limiting magnitudes of $r < 23.5$ and $i < 22.5$, over effective areas of 140 and 168 square degrees, respectively.

3 MODEL FOR THE LENSING AND SYSTEMATIC ERROR SIGNALS

We model the observed galaxy shape field as the sum of a cosmic shear component, an independent systematics field produced by anisotropies in the effective PSF e_{psf} , and a systematics field produced by the intrinsic spatial correlations of galaxy shapes e_{int} (intrinsic alignments; e.g. Hirata & Seljak 2004). For this work, we follow Bernstein & Jarvis (2002) and define shapes as ‘distortions’, which are related to the axis ratio q of an ellipse as

$$|e| = \frac{1 - q^2}{1 + q^2} \quad (2)$$

¹ <https://www.darkenergysurvey.org/>

² <http://www.astro-wise.org/projects/KIDS/>

³ <http://pan-starrs.ifa.hawaii.edu/public/>

⁴ <http://www.lsst.org/lsst>

⁵ <http://sci.esa.int/science-e/www/area/index.cfm?fareaid=102>

⁶ <http://wfirst.gsfc.nasa.gov/>

and to the adaptive second moment matrix of a surface brightness profile $I(\mathbf{x})$ as

$$e_1 = \frac{\mathbf{M}_{xx} - \mathbf{M}_{yy}}{\mathbf{M}_{xx} + \mathbf{M}_{yy}}$$

$$e_2 = \frac{2\mathbf{M}_{xy}}{\mathbf{M}_{xx} + \mathbf{M}_{yy}}, \quad (3)$$

where the adaptive moments themselves are

$$\mathbf{M}_{x_i x_j} = \int_{\infty} d^2\mathbf{x} x_i x_j w(\mathbf{x}) I(\mathbf{x}) \quad (4)$$

and w is an elliptical Gaussian weight function that has been matched in shape to the galaxy light profile.

We allow for a shear calibration factor that depends on the shear responsivity \mathcal{R} (Bernstein & Jarvis 2002) of the ensemble of galaxy surface brightness profiles to the underlying gravitationally induced shear γ . We consider \mathcal{R} to be a general factor that includes the standard response (see below) as well as any biases due to effects such as uncorrected PSF dilution, noise-related biases, or selection biases. We assume that the galaxy shape response to PSF anisotropies \mathcal{R}_{psf} is not a priori known, but rather suffers from a similar set of ‘calibration’ uncertainties as the response of the ensemble of galaxy images to gravitational lensing shear. Thus we define our model for the two ellipticity components $\mathbf{e} = (e_1, e_2)$ as

$$\mathbf{e} = \mathcal{R}\gamma + \mathcal{R}_{\text{psf}}\mathbf{e}_{\text{psf}} + \mathbf{e}_{\text{int}}. \quad (5)$$

We assume that the two-point statistics of the underlying (cosmological) shear field $\langle\gamma\gamma\rangle$ consist entirely of E-modes, $e_{\gamma,E}$ (which is a good enough approximation given the size of our errors; Crittenden et al. 2002; Schneider, van Waerbeke & Mellier 2002), and are statistically independent of the PSF when averaged over large regions. We also assume that the PSF and the intrinsic alignments are independent – but not that the lensing shear and intrinsic alignments are independent (Hirata & Seljak 2004). The two-point correlation of the galaxy shapes contains terms resulting from gravitational lensing and from systematic errors

$$\langle\mathbf{e}\mathbf{e}\rangle = \mathcal{R}^2\xi_{\gamma,E} + \mathcal{R}_{\text{psf}}^2\xi_{\text{psf}} + \xi_{\text{int}} + \langle\mathbf{y}\mathbf{e}_{\text{int}}\rangle. \quad (6)$$

Here, ξ_{psf} is the autocorrelation of the PSF ellipticity field. Errors in the determination of the galaxy redshift distribution will enter as a bias in the predicted $\xi_{\gamma,E}$.

Our goal is to carry out a statistics-limited measurement of $\xi_{\gamma,E}$. This will entail showing that the combined amplitudes of $\mathcal{R}_{\text{psf}}^2\xi_{\text{psf}}$, ξ_{int} , $\langle\mathbf{y}\mathbf{e}_{\text{int}}\rangle$, the uncertainty in the theoretically predicted $\xi_{\gamma,E}$ arising from redshift errors, and the uncertainty in the shear calibration (via the responsivity \mathcal{R}) contribute less than 20 per cent to the statistical errors in $\langle\mathbf{e}\mathbf{e}\rangle$.

Our approach to handling of systematic error is as follows: we attempt to reduce each systematic to a term that can be robustly and believably estimated from real data (either the data here or in other, related work), and we then explicitly correct for it. These corrections naturally have some uncertainty associated with them, which we use to derive a systematic error component to the covariance matrix. The exception to the rule given here is if there is a systematic error for which there is no clear path to estimating its magnitude, then we do not attempt any correction, and simply marginalize over it by including an associated uncertainty in the covariance matrix.

3.1 Cosmic shear

Foreground anisotropies in the matter distribution along the line of sight to a galaxy will generically distort the galaxy image. For weak

lensing, the leading order lensing contribution to galaxy shapes can be thought of as arising from a linear transformation of the image coordinates $\mathbf{A}\mathbf{x}_{\text{true}} = \mathbf{x}_{\text{obs}}$, where

$$\mathbf{A} = \begin{pmatrix} 1 + \kappa + \gamma_1 & \gamma_2 \\ \gamma_2 & 1 + \kappa - \gamma_1 \end{pmatrix}. \quad (7)$$

The convergence κ causes magnification, whereas the shear components γ_1 and γ_2 map circles to ellipses. The shear is related to the projected line-of-sight matter distribution, weighted by the lensing efficiency

$$(\gamma_1, \gamma_2) = \partial^{-2} \int_0^{\infty} W(\chi, \chi_i) (\partial_x^2 - \partial_y^2, 2\partial_x\partial_y) \delta(\chi\hat{\mathbf{n}}_i) d\chi. \quad (8)$$

Here we integrate along the comoving line-of-sight distance χ (where χ_i is the distance to the source), and the matter overdensity $\delta = (\rho - \bar{\rho})/\bar{\rho}$. The window function in a flat universe is

$$W(\chi, \chi_i) = \frac{3}{2}\Omega_m H_0^2 (1+z)\chi^2 \left(\frac{1}{\chi} - \frac{1}{\chi_i} \right). \quad (9)$$

The 2-point correlation function (2PCF) of the shear can be calculated by identifying pairs of source galaxies, and defining shear components (γ_i, γ_s) for each one to be the shear in the coordinate system defined by the vector connecting them, and in the $\pi/4$ rotated system. This 2PCF can be expressed as a linear transformation of the matter power spectrum P_δ averaged over the line of sight to the sheared galaxies

$$\xi_{\pm} = \langle\gamma_i\gamma_i\rangle \pm \langle\gamma_i\gamma_s\rangle$$

$$= \frac{1}{2\pi} \int_0^{\infty} d\ell \ell P_\kappa(\ell) J_{0,4}(\ell\theta) \quad (10)$$

and

$$P_\kappa = \left(\frac{3\Omega_m}{2d_H^2} \right) \int_0^{\infty} \frac{d\chi}{a(\chi)^2} P_\delta \left(\frac{\ell}{d(\chi)} \right)$$

$$\times \left[\int_{\chi'}^{\infty} d\chi' n(\chi') \frac{d(\chi' - \chi)}{d(\chi')} \right]^2, \quad (11)$$

where the last expression makes use of Limber’s approximation and $d(\chi)$ is the distance function, i.e. χ in a flat universe, $K^{-1/2} \sin K^{1/2}\chi$ in a closed universe, and $(-K)^{-1/2} \sinh(-K)^{1/2}\chi$ in an open universe. In the expression in brackets, $n(\chi')$ represents the source distribution as a function of line-of-sight distance (normalized to integrate to 1). This statistic (P_κ) is sensitive both to the distribution of matter δ and to the background cosmology, via both the explicit Ω_m dependence and the distance–redshift relations.

3.2 Intrinsic alignments

Many studies have discussed intrinsic alignments of galaxy shapes due to effects such as angular momentum alignments or tidal torque due to the large-scale density field (for pioneering studies, see Croft & Metzler 2000; Heavens, Refregier & Heymans 2000; Catelan, Kamionkowski & Blandford 2001; Crittenden et al. 2001; Jing 2002; Hopkins, Bahcall & Bode 2005). While these effects can generate coherent intrinsic alignment two-point functions, Hirata & Seljak (2004) pointed out that the large-scale tidal fields that can cause intrinsic alignments are sourced by the same large-scale structure that is responsible for producing a cosmic shear signal. Thus, in this model, the intrinsic alignments do not just have a non-zero autocorrelation, they also have a significant anticorrelation with the lensing shear which can persist to very large transverse scales and

line-of-sight separations. If left uncorrected, this coherent alignment of intrinsic galaxy shapes suppresses the lensing signal, since the response of the intrinsic shape to an applied tidal field has the opposite sign from the response of the galaxy image to a shear with the same magnitude and direction. We generally refer to the intrinsic alignment autocorrelation as the ‘II’ contamination and its correlation with gravitational lensing as the ‘GI’ contamination. This can be compared to the pure gravitational lensing autocorrelation (‘GG’).

To address the uncertainty related to intrinsic alignments, we rely on empirical measurements that constrain the degree to which they might affect our measurement. Several studies using SDSS imaging and spectroscopic data (e.g. Mandelbaum et al. 2006a; Hirata et al. 2007; Okumura, Jing & Li 2009; Joachimi et al. 2011; Mandelbaum et al. 2011) have demonstrated the existence of intrinsic alignments of galaxy shapes on cosmological distance scales. Hirata et al. (2007) used the luminosity and colour dependence of intrinsic alignments for several SDSS galaxy samples to estimate the contamination of the cosmic shear signal due to intrinsic alignments for lensing surveys as a function of their depth. These estimates were a function of the assumptions that were made, for example about evolution with redshift. The ‘central’ model given in that paper leads to a fractional contamination of

$$\frac{C_{\ell=500,GI}}{C_{\ell=500,GG}} \approx -0.08 \quad (12)$$

for a limiting magnitude of $m_{R, \text{lim}} = 23.5$, which is close to the limiting magnitude of our sample. Subsequent work (Joachimi et al. 2011; Mandelbaum et al. 2011) provided more information about redshift evolution; primarily those results were in broad agreement with the previous ones, and were sufficient to rule out both the ‘very optimistic’ and the ‘pessimistic’ models in Hirata et al. (2007).

We thus adopt the ‘central’ model, and apply the correction given in equation (12) to our theory predictions for the C_{ℓ} due to cosmic shear, multiplying the predicted cosmic shear power spectrum by 0.92 before transforming into the statistics that are used for the actual cosmological constraints⁷ (Mandelbaum et al. 2011).

All of these analyses constrain the amplitude, scale dependence, and redshift evolution of the intrinsic alignment signal in red galaxies; none, however, have provided more than an upper limit to the intrinsic alignment signal arising from blue galaxies. The selection functions in each case in redshift, colour, and morphology will differ from that for this analysis. Nevertheless, the existing work provides useful limits on the fraction of intrinsic alignment contamination in the cosmic shear signal measured here.

For red galaxies, the GI signal is well measured in the redshift range considered here. The Joachimi et al. (2011) results constrain the contamination fraction to 33 per cent. For blue galaxies, Mandelbaum et al. (2011) provide upper limits constraining the contamination for a roughly similar survey to 10 per cent or less. The latter measurement includes only very blue galaxies, and in the absence of a more representative measurement at these redshifts we round the total fractional error up to 50 per cent, which is much larger than the uncertainty in the measured GI contamination from Joachimi et al. (2011) and amounts to an overall 4 per cent uncertainty in the theory prediction (see Section 5 for a quantitative description of how we incorporate this and other systematic uncertainties into the

covariance matrix). It is difficult to adopt more rigorous errors in the absence of further empirical constraints on intrinsic alignments for galaxy populations similar to those studied here; fortunately, as we show below, even this conservative uncertainty is small compared to the errors in the final cosmic shear measurement.

Since the GI correlation is first order in the intrinsic alignment amplitude, while the II power is second order, we expect the first to be the dominant systematic. In principle, the GI effect could be smaller than II if the correct alignment model is quadratic in the tidal field rather than linear (Hirata & Seljak 2004). However, in the aforementioned cases in which intrinsic alignment signals are detected at high significance (i.e. for bright ellipticals) the linear model for intrinsic alignments appears to be valid (Blazek, McQuinn & Seljak 2011). Therefore, we attempt no correction for II.

3.3 Shear calibration

Another source of systematic error for weak lensing measurements is uncertainty in the *shear calibration* factor. The galaxy ellipticity (e_+ , e_{\times}) observed after isotropizing the PSF need not have unit response to shear: in general, averaged over a population of sheared galaxies, we should have

$$\langle (e_+, e_{\times}) \rangle = \mathcal{R}(\gamma_+, \gamma_{\times}), \quad (13)$$

where \mathcal{R} is the shear responsivity. It depends on both the shape measurement method *and* the galaxy population (e.g. Massey et al. 2007b; Bernstein 2010; Zhang & Komatsu 2011).

For this work, we used the re-Gaussianization method (Hirata & Seljak 2003), which is based on second moments from fits to elliptical Gaussians, and has been previously applied to SDSS single-epoch imaging (Mandelbaum et al. 2005; Reyes et al. 2012). For this class of methods, in the absence of selection biases and weighting of the galaxies, perfectly homologous isophotes, and no noise, there is an analytic expectation (Bernstein & Jarvis 2002)

$$\mathcal{R} = 2(1 - e_{\text{rms}}^2), \quad (14)$$

where e_{rms} is the root-mean-square (rms) ellipticity per component (+ or \times).

The calibration errors for re-Gaussianization and other adaptive-weighting methods are well studied in the literature (e.g. Hirata et al. 2004b; Mandelbaum et al. 2005; Reyes et al. 2012). They arise from all of the deviations from the assumptions of equation (14). Higher order⁸ departures from non-Gaussianity in the galaxy light profile cause errors in the PSF dilution correction. Errors in the measurement of the PSF model will cause a similar error in the dilution correction. The resolution factor of an individual galaxy depends on its ellipticity, so any resolution cut on the galaxy sample will introduce a shear bias in the galaxy selection function. Due to the non-linearity of the shear inference procedure, noise in the galaxy images causes a bias in the shears (rather than just making them noisier). The estimation of the shear responsivity, or even of e_{rms} , is another potential source of error, as the response of the galaxies to the shear depends on the true, intrinsic shapes, rather than the gravitationally sheared, smeared (by the PSF), noisy ones that we observe.

Past approaches to this problem have included detailed accounting for these effects one by one. In this paper, we instead use

⁷ While the intrinsic alignment contamination is in principle scale dependent, the plots in Hirata et al. (2007) suggest that this scale dependence is in fact quite weak for the scales used for our analysis, so we ignore it here.

⁸ Non-zero higher order terms in the elliptical Gauss-Laguerre expansion of the galaxy light profile; see Hirata & Seljak (2003) for details.

detailed simulations of the image processing and shape measurement pipelines, including real galaxy images, to estimate both the shear calibration and the redshift distribution of our catalogue. The advantage is that this includes all of the above effects and avoids uncertainties associated with analytic estimates of errors. The SHERA Reconvolution Analysis (SHERA) simulation package⁹ has been previously described (Mandelbaum et al. 2012) and applied to single-epoch SDSS data for galaxy–galaxy lensing (Reyes et al. 2012), but this is its first application to cosmic shear data.

To simulate our images, we require a fair, flux-limited sample of any galaxies that could plausibly be resolved in our co-add imaging, including high-resolution images with realistic morphologies.¹⁰ For this purpose we use a sample of 56 662 galaxy images drawn from the COSMOS (Koekemoer et al. 2007; Scoville et al. 2007a,b) imaging catalogues. The deep *Hubble Space Telescope* (HST) Advanced Camera for Surveys (ACS)/Wide Field Camera imaging in *F814W* (‘broad *I*’) in this 1.6 deg² field is an ideal source of a fairly selected galaxy sample with high resolution, deep images.¹¹ These images consist of two samples – a ‘bright’ sample of 26 116 galaxies in the magnitude range $I < 22.5$, and a ‘faint’ sample consisting of the $22.5 < I < 23.5$ galaxies. The charge transfer inefficiency-corrected (Massey et al. 2010) and multidrizzled (Koekemoer et al. 2002; Rhodes et al. 2007, to a pixel scale of 0.03 arcsec) galaxy postage-stamp images have been selected to avoid CCD edges and diffraction spikes from bright stars, and have been cleaned of any other nearby galaxies, so they contain only single galaxy images without image defects. The bright sample is used for ground-based image simulations in Mandelbaum et al. (2012); the faint sample is selected and processed in an identical way.¹² Each postage stamp is assigned a weight to account for the relative likelihoods of generating postage stamps passing all cuts (avoidance of CCD edges and bright stars) for galaxies of different sizes in the COSMOS field; this weight is calculated empirically, by comparing the size distribution of galaxies with postage stamps to the size distribution of a purely flux-limited sample of galaxies.

Each of these postage-stamp images has several properties associated with it that are of interest for this analysis. The COSMOS photometric catalogues (Ilbert et al. 2009) contain *HST F814W* magnitudes as well as photometric redshifts and *Subaru r – i* colours based on PSF-matched aperture magnitudes.

In order to simulate our observations, we first select a co-add ‘run’ consisting of five adjacent frames in the scan direction at random from the list of completed runs. We draw 1250 galaxies (exactly 250 per frame) at random from the list of COSMOS postage stamps according to the weights described above, up-weighting the probability of drawing the faint galaxies by a factor of 1.106 to account for the fact that we have sampled the faint population at a lower rate than the bright one in constructing the image sample.

Once a list of postage-stamp images is selected, we assign *r*- and *i*-band magnitudes by re-scaling each image; each galaxy image is inserted into the co-added imaging with the flux it would have been observed to have in SDSS before the addition of pixel noise.

The *i* band is chosen to be 0.03 mag brighter than the COSMOS *F814W* (*I*) band MAG_AUTO values; this small offset is based on empirical comparison with SDSS magnitudes for brighter galaxies, to account for slight differences in the *F814W* and *i* passbands (Mandelbaum et al. 2012). The *r* band is chosen so as to match the *Subaru* PSF-matched aperture colours for each object. Each postage stamp is assigned a random, uniformly sampled position in the co-add run, with the postage stamps distributed equally among the frames.

We use the SHERA code to pseudo-deconvolve the *HST* PSF, apply (if necessary; see below) a shear to each galaxy, reconvolve each image with the known co-add PSF, renormalize the flux appropriately, and resample from the COSMOS pixel scale to the co-add pixel scale before adding that postage stamp to the co-add image. This procedure, suggested by Kaiser (2000) and implemented to high precision in Mandelbaum et al. (2012), can be used to simulate ground-based images with a shear appropriately applied, despite the space-based PSF in the original COSMOS images, and with a user-defined PSF.

The normal co-add masking algorithm is then applied, and shear catalogues are generated as in Paper I by running the SDSS object detection and measurement pipeline, PHOTO-FRAMES, followed by the shape measurement code described in Paper I. The output catalogues are matched against the known input object positions, and a simulation catalogue of the matches is created. We employ these simulations below to determine the shear calibration and as an independent validation of our inferred redshift distribution.

For each suite of simulation realizations, we use the same random seed (i.e. we select the same galaxies from our catalogue and place them at identical locations in the co-added image) but with different applied shears per component ranging from -0.05 to $+0.05$. We measure the mean weighted shape of the detected simulation galaxies produced by our pipeline, and fit a line to the results. Since the same galaxies are used without rotation, only the slope and not the intercept is meaningful. The shear response in each component for each applied shear is shown in Fig. 1. The responsivities in the two components are consistent, which is expected on oversampled data with a rounded PSF. (The unequal size of the error bars reflects the number of runs that we were able to process by the time the shear calibration solution was frozen.) The total number of galaxies in the final simulated catalogues was 130 063. The response appears to be linear for small applied shears. Based on these results, we adopt a shear responsivity for this galaxy population of 1.776 ± 0.043 . For the galaxy population used in this measurement, the shape dispersion e_{rms} is 0.37; the corresponding responsivity for an unbiased shape measurement method, by equation (14), is 1.72. Even in the absence of any correction from the simulations above, this measurement would only suffer a 2.8 per cent shear calibration bias, which is already an unusually small bias given that it includes many realistic effects such as selection bias, noise rectification bias, and effects due to realistic galaxy morphologies. This bias is well below the statistical errors of our measurement, but we correct for it in any case by using the simulation-based responsivity rather than the ‘ideal’ one based on the rms ellipticity.

3.4 Redshift distribution

The explicit dependence of the shear signal in equations (8) and (11) on the distribution of lensed galaxy redshifts, combined with the practical impossibility of acquiring a spectroscopic redshift for the millions of faint galaxies statistically necessary for a cosmic shear

⁹ <http://www.astro.princeton.edu/~rmandelb/shera/shera.html>

¹⁰ Simple models with analytic radial profiles and elliptical isophotes are not adequate to measure all sources of systematic error such as under-fitting biases or those due to non-elliptical isophotes (Bernstein 2010).

¹¹ Admittedly there may be some sampling variance that affects the morphological galaxy mix.

¹² We thank Alexie Leauthaud for kindly providing these processed images.

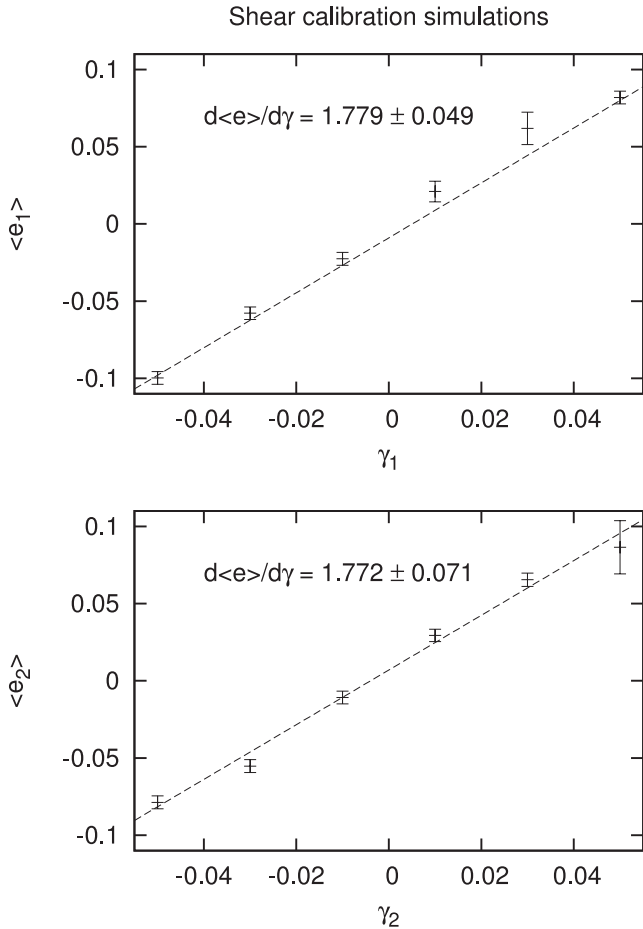


Figure 1. The response of the mean ellipticities (e_1) and (e_2) to applied shear, as determined in the SHERA-based simulations. Poisson error bars are shown. The additive offset to the response curve is not shown in the fit; these simulations do not accurately measure an additive shear bias.

measurement, can be a troublesome source of bias and systematic uncertainty for cosmic shear measurements.

An error in the estimated redshift distribution leads to an incorrect prediction for the amplitude of the shear signal at a given cosmology. This is similar in principle to the bias arising in the amplitude of the galaxy–galaxy lensing signal due to photometric redshift biases explored in Nakajima et al. (2011); uncorrected, standard photometric redshift estimation techniques can lead to biases in the predicted lensing signal at the ~ 10 per cent level. For cosmic shear measurements, an imperfect estimate of the redshift distribution leads to biases in σ_8 and Ω_m that are comparable in amplitude to the errors in the estimated mean of the redshift distribution (van Waerbeke et al. 2006).

As a fiducial reference, the redshift distribution of the single-epoch SDSS imaging catalogue is established to approximately 1 per cent (Sheldon et al. 2011); for deeper surveys over a smaller area, this becomes a more difficult problem, as the spectroscopic calibration samples available for inferring the redshift distribution are limited in their redshift coverage and widely dispersed across the sky. We employ a colour-matching technique similar to that employed by Sheldon et al. (2011); in what follows, we describe the technique, our estimate of its uncertainty, and several cross-checks on the results.

3.4.1 Fiducial redshift distribution

The source redshift distribution used in our analysis is derived following Lima et al. (2008) and Cunha et al. (2009), and is similar in spirit to Sheldon et al. (2011); the principle is that, for two galaxy samples that span broadly similar ranges in redshift, colour, and limiting magnitude, matched colour samples correspond to matched redshift distributions.

Our spectroscopic calibration sample is composed of 12 360 galaxies, from the union of the VISIBLE MultiObject Spectrograph Very Large Telescope Deep Survey (VVDS; Le Fèvre et al. 2005) 22 h field, the DEEP2 Galaxy Redshift Survey (Davis et al. 2003; Madgwick et al. 2003), and portions of the PRIMUS Multi-object Survey (PRIMUS; Coil et al. 2011; Cool et al. 2013). We follow the procedures outlined in Nakajima et al. (2011) for selecting good quality spectroscopic redshifts, and avoiding duplicate galaxies in samples that overlap (such as DEEP2 and PRIMUS). Each of these samples has a redshift distribution that is likely to differ substantially from the redshift distribution of our lensing catalogue: the DEEP2 catalogue in the fields we use at $23^{\text{h}}30^{\text{m}}$ and $02^{\text{h}}30^{\text{m}}$ is heavily colour selected (in non-SDSS bands) towards objects at $z > 0.7$; the PRIMUS catalogue includes several fields, some of which are selected from imaging with a shallower limiting magnitude; and the VVDS catalogue is selected in the I band ($I < 22.5$) with a relatively high-redshift failure rate that exhibits some colour dependence.

We assign a redshift from a galaxy in the union calibration sample to the closest galaxy in the lensing catalogue within 3 arcsec, finding 12 360 matches. To generate a representative training sample of galaxies from the lens catalogue, we draw 4×10^5 galaxies with replacement from the full area (not just in these regions), with sampling probability proportional to the mean of the weights assigned in the r and i bands to that galaxy for the correlation analysis (equation 22). Note that this procedure does not incorporate those galaxies in the excluded camcol 2 region.

We use the Lima et al. (2008) code¹³ to solve for a set of weights over the calibration sample, such that the re-weighted 5D magnitude distributions of the calibration sample match those of the representative random subset of the lensing catalogue.

All photometric redshift estimation methods (at least implicitly) that two galaxy populations with similar distributions in colour and magnitude have similar distributions in redshift. If that is the case, and if the spectroscopic sample spans the full range of properties of the photometric sample, then the photometric distribution over the vector of galaxy properties \mathbf{p} (in this case, 5-band SDSS magnitudes) $n_p(\mathbf{p})$ can be written as a product of the true spectroscopic redshift distribution and a redshift-dependent function:

$$n_p(\mathbf{p}) = n_s(\mathbf{p})w(\mathbf{p}). \quad (15)$$

The algorithm attempts to find a weight $w(\mathbf{p}_i)$ for the i th galaxy such that the histogram of the re-weighted spectroscopic calibration sample has the same properties as a fair sample of the true redshift distribution of the photometric sample. It uses a nearest-neighbour method to define volume elements in 5-band magnitude space such that for any given volume element, the galaxies in that element can be assigned a weight $w(\mathbf{p}) = n_p(\mathbf{p})/n_s(\mathbf{p})$ without the ratio introducing unmanageable amounts of noise. Summing the re-weighted n_s over the property vector in a single redshift bin yields an estimate of the n_p .

¹³ <http://kobayashi.physics.lsa.umich.edu/~ccunha/nearest/>

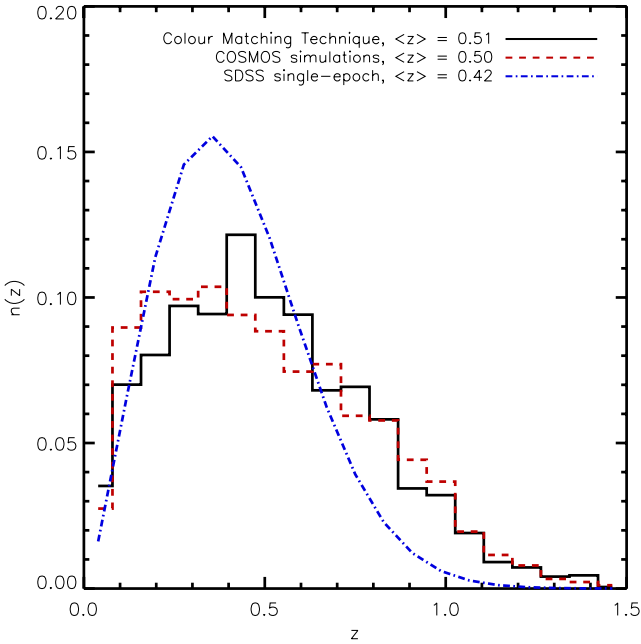


Figure 2. The redshift distribution inferred from matching the colours of the spectroscopic calibration sample to those of the lensing catalogue (solid black line, Section 3.4.1) shown alongside the noisier redshift distribution inferred from the shear calibration simulations (dashed red line, Section 3.4.3). The best-fitting distribution for the single-epoch SDSS lensing catalogue from Nakajima et al. (2011) is shown for reference as the blue dot-dashed line.

Because the COSMOS tests described below agree perfectly (within statistical errors) with the redshift histogram, major biases are extremely unlikely – such biases would require a significant population of galaxies at $z < 1$ for which no spectroscopic redshifts in PRIMUS, VVDS, or DEEP2 are successful, and which are also invisible to any checks on the COSMOS photo- z 's. While not impossible, the existence of such a population in this sample seems improbable.

The histogram of the calibration sample redshifts reweighted in this manner is shown as a solid line in Fig. 2. The inferred mean redshift is 0.51; in contrast to the redshift distribution for single-epoch imaging, there is a non-negligible fraction of the galaxy sample above $z > 0.7$. We use the solid curve based on the colour-matching techniques to calculate the shear covariance matrix, and to predict the shear correlation function for any given cosmology.

3.4.2 Uncertainty

We expect that the primary source of error in the redshift distribution as estimated from the combined calibration sample is sample variance, resulting from the finite volume of the calibration sample. To estimate its magnitude, we use the public code of Moster et al. (2011) for estimating the cosmic variance of number counts in small fields.

Our redshift binning scheme has 19 bins between $0 < z < 1.5$. For a collection of disparate calibration fields, we use the Moster et al. (2011) code to produce a fractional error in the number counts $\sigma_{\text{gg}, i, j}$ for the j th redshift bin in the i field (where fields are distinguished by their coverage area) in bins of stellar mass.

The redshift sampling rate of each distinct survey in the calibration sample differs, and so the balance of contributions to the final redshift distribution will change as well. To account for this, we sum

over every calibration field's contribution to the reweighted redshift distribution in the j bin to estimate an absolute (not relative) overall error

$$\sigma_j^2 = \sum_i (\sigma_{\text{gg}, i, j} n_{\text{eff}, i, j})^2, \quad (16)$$

where the effective number of galaxies contributed in the j bin by the i survey is just the sum over the nearest-neighbour derived weights assigned to calibration sample galaxies k in that field i and bin j :

$$n_{\text{eff}, i, j} = \sum_k w_{nn, i, j, k}. \quad (17)$$

To propagate these errors into the covariance matrix for ξ_E , we first fit a smooth function of the form

$$n_z(z) \propto z^a e^{-(z/z_0)^b} \quad (18)$$

to the nearest-neighbour weighting-derived redshift distribution shown in Fig. 2; the best-fitting parameters are $a = 0.5548$, $z_0 = 0.7456$, and $b = 2.5374$. We perturb this smooth distribution by adding a random number drawn from a normal distribution with mean $n_z(z_j)$ (normalized to the weighted number of calibration galaxies in that bin) and standard deviation σ_j at the location of the j th redshift bin. We then renormalize the perturbed distribution to unity, and compute the predicted cosmic shear signal. The covariance matrix of 402 realizations of this procedure is added to the statistical covariance matrix.

3.4.3 Other tests

As an independent check on the redshift distribution, we also use the shear calibration simulations (Section 3.3) to constrain the redshift distribution of our sources. The COSMOS photometric redshifts, inferred as they are from many more imaging bands (typically with deeper imaging) than for the SDSS data discussed here, are very accurate. For example, Ilbert et al. (2009) find a photo- z scatter of $\sigma_z/(1+z) \sim 0.01$ for a galaxy sample with the flux limit of the SDSS co-adds. In contrast, Nakajima et al. (2011) found that in the SDSS single-epoch imaging, the scatter defined in the same way was ~ 0.1 despite the brighter flux limit of the single-epoch imaging (due in part to the more limited number of bands, but primarily to the far lower signal-to-noise ratio). If we treat the COSMOS photometric redshifts as we would treat the spectroscopic data, then the redshift distribution of COSMOS galaxies that pass successfully into the shear catalogue is the same as that of our source catalogue – assuming, of course, that the COSMOS field is representative of the whole of Stripe 82. It is not, of course; large-scale structure in the COSMOS field (which can be significant, as COSMOS covers only 1.7 square degrees; Kovač et al. 2010) can bias a determination of the redshift distribution in this manner. The $n(z)$ inferred from the COSMOS-based simulations is also shown in Fig. 2, and agrees extremely well with the fiducial $n(z)$ derived from colour matching.

A final (but obviously not independent) sanity check is to compare to the COSMOS Mock Catalogue (Jouvel et al. 2009), which is being used extensively to plan future dark energy programmes, using the cuts $r_{\text{eff}} > 0.47$ arcsec, limiting magnitudes $r < 23.5$, and $i < 22.5$ (see Paper I, where we argue that these most closely mimic the cuts in our data). This test predicts $\langle z \rangle = 0.51$, identical to that obtained via the re-weighting procedure. Given the crudeness of the procedure for comparing the results, this is an excellent validation of the COSMOS Mock Catalogue as a forecasting tool.

Redshift deserts that arise from the lack of identifiable emission lines in the observed wavelength window are common between surveys; it is difficult to check, based on the data in hand, whether this is a significant effect for our redshift distribution inference method. It should be noted, however, that the redshift desert for the DEEP2 sample, which constrains the high-redshift tail of our sample, occurs between $1.4 < z < 1.7$, which is too high to have much effect on the shallow SDSS imaging.

3.4.4 Redshift-dependent shear calibration bias

Systematic variations in the shear calibration with galaxy properties are a generic feature of shape measurement (Massey et al. 2007a; Bernstein & Huterer 2010; Zhang & Komatsu 2011; Mandelbaum et al. 2012). This arises not only from evolution in the properties of galaxy morphologies with redshift, but from noise biases (as more distant galaxies tend to be fainter) and from selection biases (as it is impossible to select galaxies in a manner that is independent of the shear). Analytic estimates of the sizes of these latter two effects suggest that they can be important at the 10 per cent level (Hirata & Seljak 2003; Mandelbaum et al. 2005). Even state-of-the-art methods show calibration biases that depend strongly (i.e. at the ≈ 10 per cent level) on resolution and signal-to-noise ratio (Miller et al. 2013).

The two-point shape correlation functions used for this analysis average over the entire shape catalogue, so a redshift-dependent shear calibration will result in a bias in the overall shear amplitude if we do not correct for it properly. Here we describe tests for such an effect.

To estimate the magnitude of this systematic error, we split the shape catalogues generated by the COSMOS simulations described above at the mean of the redshift distribution of the detected simulation catalogue, and measure the effective shear calibration factors of the low- and high-redshift segments of the simulated catalogue to be $\mathcal{R}_{\text{low-}z} = 1.60$ and $\mathcal{R}_{\text{high-}z} = 2.0$, respectively. This is a large shift in the calibration factor, and while it is not inconsistent with the typical magnitude of selection effects and noise rectification biases, as discussed above, it does merit further investigation. Using the shear prediction code detailed in Section 6.1, we compare the cosmological predictions using the *WMAP7* Λ CDM parameters adopted as fiducial in Section 5.1.2 and a mean calibration factor 1.776 to predictions generated by the same cosmology, but applying the two calibration factors $\mathcal{R}_{\text{low-}z}$ and $\mathcal{R}_{\text{high-}z}$ to the signal from the low- and high- z halves of the redshift distribution. The change in the amplitude of the predicted signal (shown in Fig. 3) is at most 2.25 per cent. We define the distance between these two predictions in statistical significance as

$$\text{distance} = \sqrt{\Delta_i [\mathbf{C}^{-1}]_{ij} \Delta_j} \quad (19)$$

where Δ_j is the difference between the Complete Orthogonal Sets of E-/B-mode Integrals (COSEBI) vectors generated by using the varying redshift-varying shear calibration factors described above and the single mean calibration factors used in the rest of the analysis. We find $\text{distance} = 0.005838667$, whereas a statistically significant effect would have an order-unity effect on the distance. As the redshift-dependent shear calibration bias does not appear to have a noticeable impact on the cosmological parameter fits, we use the single calibration factor $\mathcal{R} = 1.776$ for the cosmological parameter analysis.

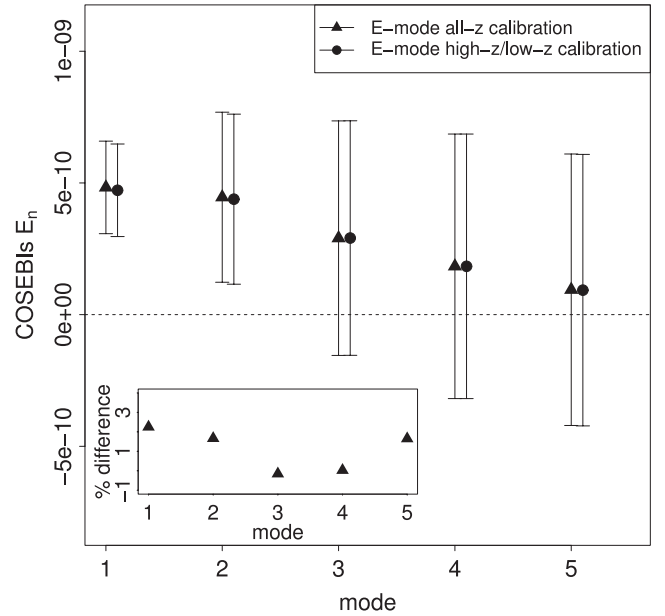


Figure 3. The effect of the redshift-dependent shear calibration on the predicted cosmic shear signal, in the COSEBI basis. Triangles show the predicted shear signal arising from using separate shear calibration factors for the high- and low-redshift halves of the simulated galaxy sample, as described in Section 3.4.4. Inset shows the per cent change in each COSEBI mode.

3.5 Stellar contamination

Stellar contamination of the galaxy catalogue reduces the apparent shear by diluting the signal with round objects that are not sheared by gravitational lensing. Because the image simulations described in Section 3.3 only included galaxies, the resulting shear responsivities do not include signal dilution due to accidental inclusion of stars in the galaxy sample. In Paper I, we estimated the stellar contamination by comparison with the DEEP2 target selection photometry (which is deeper and was acquired at the Canada–France–Hawaii Telescope under much better seeing conditions than typical for SDSS), and found a contamination fraction of 0.017. We also argued that the mean stellar density in the stripe must be larger than in the high-latitude DEEP2 fields, by a factor as large as 2.8. We therefore conservatively take the stellar contamination fraction f_{star} to be

$$f_{\text{star}} = 0.017(1.9 \pm 0.9) = 0.032 \pm 0.015. \quad (20)$$

The resulting suppression of the cosmic shear signal is treated in much the same way as for intrinsic alignments: we reduce the theory signal by a factor of $(1 - 0.032)^2 = 0.936$, and add a contribution to the covariance of 0.030 times the theory signal.

3.6 Additive systematics

Among the most worrying systematics in the early detections of cosmic shear was additive power. This comes from any non-cosmological source of fluctuations in shapes such as PSF anisotropy that add to the ellipticity correlation function of the galaxies. Such power was clearly detected in Paper I in the form of systematic variation of both star and galaxy e_1 as a function of declination. The sense of the effect – a negative contribution to e_1 (in

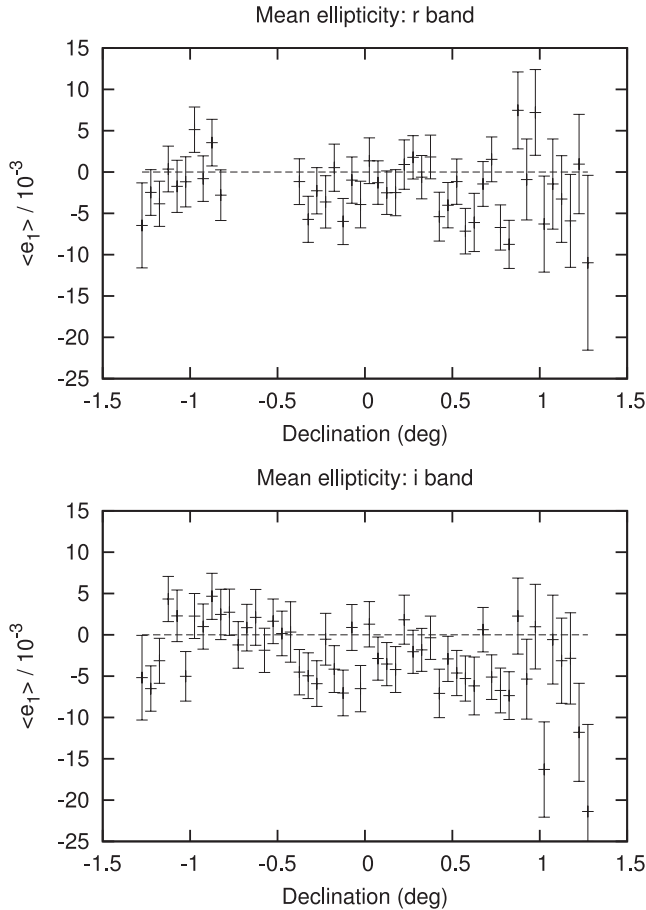


Figure 4. The mean ellipticity (e_1) as a function of declination in the r and i bands. This signal was removed from the galaxy catalogue prior to computing the final correlation function. The r -band data between declination $-0^{\circ}.8$ and $-0^{\circ}.4$ were rejected due to the known problems with camcol 2. The error bars are Poisson errors only.

band we have¹⁴ $\langle e_1 \rangle = -0.0018$ and $\langle e_2 \rangle = +0.0004$, while in i band $\langle e_1 \rangle = -0.0022$ and $\langle e_2 \rangle = -0.0002$ – is suggestive of *masking bias*, in which the selection of a galaxy depends on its orientation, with galaxies aligned in the along-scan direction ($e_1 < 0$) being favoured, and with no effect on e_2 (consistent with zero mean over the whole survey). The reason for this particular sign is seen in fig. 2 of Paper I; as shown, bad columns along the scan direction tend to be repeated at the same location in multiple images, resulting in significant (non-isotropic) masks with that directionality. Direct evidence for masking bias comes from the change in mean ellipticity due to increased masking: when we removed from the co-added image pixels that were observed in fewer than seven input runs and reran PHOTO-FRAMES, the $\langle e_1 \rangle$ signal became *worse*: -0.0051 in r band and -0.0044 in i band, whereas $\langle e_2 \rangle$ was essentially unchanged. This increase is difficult to explain in terms of spurious PSF effects, so we conclude that our galaxy catalogue likely contains a mixture of masking bias as well as possible additive systematics from PSF ellipticity in the co-added image.

The mean e_1 signal as a function of declination is shown in Fig. 4 in bins of width $0^{\circ}.05$. We take this as a template for mask-related selection biases (combined with any systematic uncorrected PSF

¹⁴ The 1σ Poisson uncertainty in these numbers is 0.0005 (0.0004) per component in r (i) band.

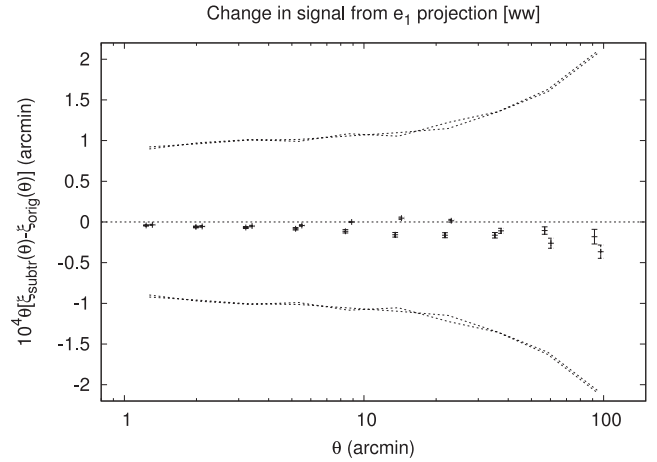


Figure 5. The loss of actual power due to e_1 projection. Using 36 realizations from the Monte Carlo simulation, we find the difference in post-projection ellipticity correlation function $\xi(\theta)$ and original $\xi(\theta)$. These are shown as the solid points (ξ_{++}) and dashed points ($\xi_{\times\times}$) in the figure, re-binned to 10 bins in angular separation θ . The dashed lines at top and bottom are the $\pm 1\sigma$ statistical error bars of our measurement. The reduction of actual power is detectable by combining many simulations, but is very small compared to the error bars on the measurement.

variation as a function of declination, which in west-to-east drift-scan observations is a highly plausible type of position dependence). *Before computing the correlation function, we subtracted this mean signal from the galaxy ellipticity catalogue.*¹⁵

One danger in this procedure to remove spurious $\langle e_1 \rangle$ is that some real power could be removed – that is, even in the absence of any systematic error, some of the actual galaxy shape correlation function signal could be suppressed since the method determines the mean e_1 of the real galaxies and by subtracting it introduces a slight artificial anticorrelation. The best way to guard against this is with simulations. Using the Monte Carlo simulation tool of Section 5.1.2, we generated simulated realizations of our ellipticity catalogue and either implemented the $\langle e_1 \rangle$ projection or not. The difference in the correlation functions is a measure of how much power was removed. The result is shown in Fig. 5, and shows that the loss of real power is insignificant compared to our error bars.

3.6.1 PSF anisotropy

Convolution with an elliptical PSF will induce a spurious ellipticity in observed galaxy surface brightness profiles. While the effective PSF for these co-adds is a circular double Gaussian to quite high precision, the tests in Paper I indicate a low level of residual anisotropy that we must consider here.

Possible sources of this issue include: (i) inaccuracies in the single-epoch PSF model used to determine the kernel to achieve the desired PSF; (ii) colour dependence of the PSF that means the single-epoch PSF model from the stars is not exactly the PSF for the galaxies; or (iii) the fact that we determine the rounding kernel on a fixed grid, so that smaller scale variations in PSF anisotropy might remain uncorrected. All of these must be present at some level, although the last two cannot be the full solution: (ii) does not

¹⁵ We refer below to this step as projection, as the intent is to map the shape catalogue on to a subspace of itself that does not include the spurious masking-induced modes.

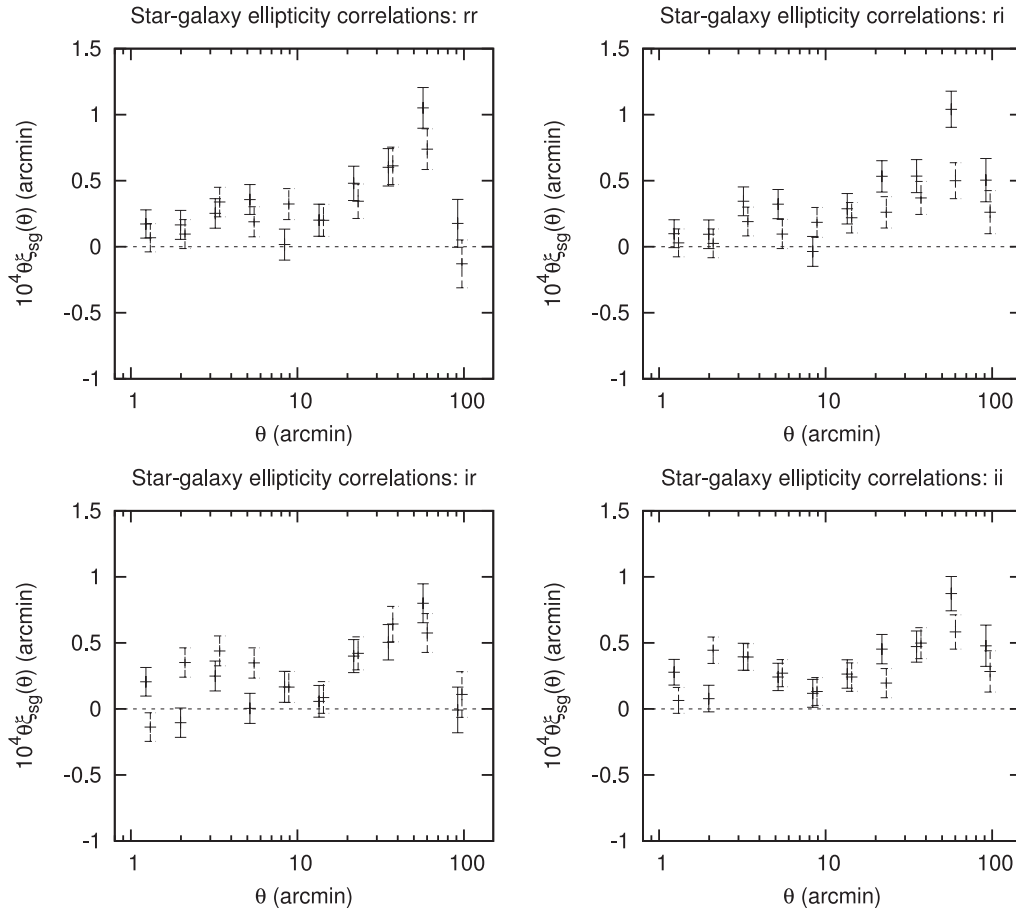


Figure 6. The star–galaxy ellipticity correlation functions. Shown are the rr , ri (i.e. star $r \times$ galaxy i), ir , and ii correlation functions, reduced to 10 bins. The solid points, which are offset to slightly lower θ values for clarity, are the $++$ correlation functions, and the dashed points are the $\times\times$ functions. All error bars are Poisson only.

explain the residual stellar ellipticity¹⁶ and (iii) does not explain why there is structure in the declination direction on the scale of an entire CCD (0:23).

For a galaxy and a PSF that are both well approximated by a Gaussian, the PSF correction given above produces a measured ellipticity of

$$e^{\text{obs}} = \mathcal{R}_{\text{psf}} e^{\text{PSF}} = \frac{1 - R_2}{R_2} e^{\text{PSF}}, \quad (21)$$

see e.g. Bernstein & Jarvis (2002). The weighted (by the same weights used for the correlation function; see equation 22) average of the PSF anisotropy response defined in equation (21) over the sample of galaxies considered in this work is $\mathcal{R}_{\text{psf}} = 0.86$ (r band) or 0.95 (i band); in what follows we take a value of 0.9.

A non-zero star–galaxy correlation function ξ_{sg} resulting from systematic PSF anisotropy (as estimated in Paper I) indicates the presence of a spurious contribution to the shear–shear correlation function with amplitude $\approx 0.9\xi_{\text{sg}}$. We will not determine this response to high-enough accuracy to subtract the effect with small residual error: doing so would not require just a simulation, but a

simulation that knows the correct radial profile of the PSF errors.¹⁷ In our case, the star–galaxy correlation function is detectable but below the errors on the galaxy–galaxy ellipticity autocorrelation (although not by very much), so a highly accurate correction is unnecessary.

We constrain the PSF anisotropy contribution by computing the star–galaxy correlation function. This was done in Paper I, but some of the star–galaxy signal is due to the systematic variation of PSF ellipticity with declination and is removed by the subtraction procedure above. The star–galaxy ellipticity correlation function with the corrected catalogue is shown in Fig. 6. The implied contamination to the galaxy ellipticity correlation function, appropriately averaging the bands and applying the factor of $\mathcal{R}_{\text{psf}} = 0.9$, is shown in Fig. 7.

These measured star–galaxy correlations can be used to construct a reasonable systematics covariance matrix for this systematic. We take the amplitude of the diagonal elements of the PSF systematic covariance to be equal to the amplitude of the measured contamination. We also assume that the off-diagonal terms are fully correlated

¹⁶ We have searched for a $g - i$ dependence in the stellar ellipticities in the co-added image. We only found effects at the ~ 0.002 level, and while they are statistically significant, we have not established whether they correspond to true colour dependence versus e.g. variation of stellar colour distributions along the stripe.

¹⁷ This might be an option in future space-based surveys if the type of error can be traced to the source of ellipticity (astigmatism \times defocus, coma, or jitter). In either space or ground-based data, one could imagine doing cross-correlations of higher order shapelet modes (Refregier 2003) to extract the particular form of the errors. None of these options are pursued here.

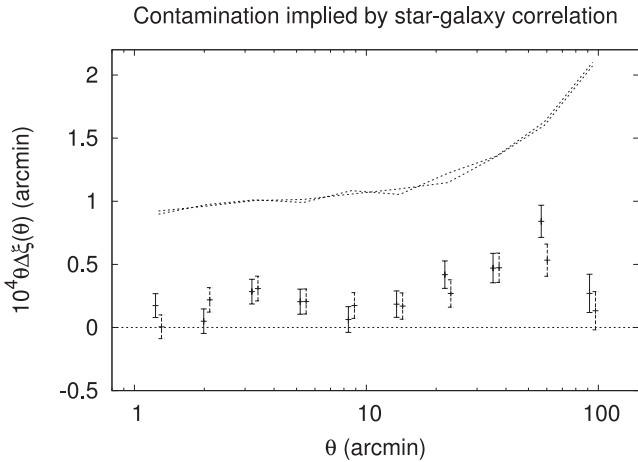


Figure 7. The implied contamination to the galaxy ellipticity correlation function if the star–galaxy correlation function is used as a measure of the additive PSF power. The solid points are the ++ correlation functions and the dashed points are the $\times\times$ functions. All error bars are propagated from the Poisson errors assuming correlation coefficient +1 (a better assumption than independent errors, but likely an overestimate). The dotted curves show the 1σ errors in each radial bin from the Monte Carlo simulations (see Section 5.1.2) which include both Poisson and cosmic variance uncertainties. Note also that the shapes and normalizations of the ++ and $\times\times$ signals are nearly identical.

between bins, which is equivalent to fixing the scaling of this systematic with radius, and saying that only the overall amplitude of the systematic is uncertain.

Since there are a number of uncertainties in this procedure, we do not apply any correction for these additive PSF systematics as we do for ones that are previously discussed, such as intrinsic alignments or stellar contamination. Instead, we simply include a term in the systematics covariance matrix to account for it. We also will present a worst-case scenario for the impact of this term on cosmological constraints; in Section 6 we will show what happens to the cosmology constraints if we assume that the systematic error is $+2\sigma$ from its mean, i.e. 40 per cent of the statistical errors. This should be taken as a worst-case scenario for this particular systematic.

One possible concern with star–galaxy correlation function test described here is that the stellar ellipticity is measured using adaptive moments at the star scale, whereas the measured galaxy ellipticities are more sensitive to the outer isophotes. We therefore repeated the star–galaxy correlation function test using the *PHOTO* moments of stars without the adaptive Gaussian weights (termed *Q* and *U*: for an object with homologous isophotes these are equivalent to e_1 and e_2).¹⁸ We take only the 80 per cent of the stars with the smallest values of $\sigma_q^2 + \sigma_u^2$, since a few objects have very large uncertainties (the *Q* and *U* moments are especially noisy for objects with highly extended ‘detected’ regions in the extracted postage stamp). The implied contamination to the galaxy ellipticity correlation function is shown in Fig. 8. By removing the Gaussian weight, we maximize sensitivity to the outer isophotes of the PSF in the co-added image. While the unweighted moments are noisier, the overall result that the additive PSF power is much smaller than the statistical errors on the cosmic shear signal is robust. In fact, with this set of moments, the star–galaxy correlation is not even detected: the χ^2 relative to

¹⁸ Here *Q* and *U* are technically defined as the intensity-weighted averages of $(x^2 - y^2)/(x^2 + y^2)$ and $2xy/(x^2 + y^2)$.

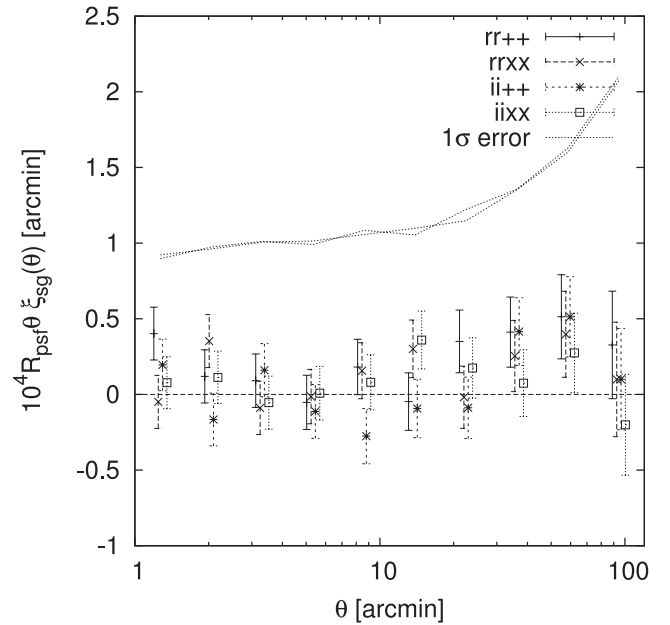


Figure 8. The implied contamination to the galaxy ellipticity correlation function if the star–galaxy correlation with no radial weight for the stars are used as a measure of the additive PSF power. That is, the points shown are $\mathcal{R}_{\text{psf}} = 0.9$ times the star–galaxy correlation, times a scaling factor of $10^4\theta$ to make the vertical axis more clearly visible. The dotted curves show the 1σ errors in each radial bin from the Monte Carlo simulations (see Section 5.1.2) which include both Poisson and cosmic variance uncertainties. The plot is noisier than Fig. 7 due to the noisier unweighted moments.

zero signal for the 10 bins shown is 13.5 ($rr++$), 9.9 ($rr\times\times$), 13.3 ($ii++$), or 6.7 ($ii\times\times$).

4 ANALYSIS TOOLS

4.1 Ellipticity correlation function

We compute the ellipticity correlation functions defined in equation (10) on scales from 1–120 arcmin. For the cosmological analysis, we start by computing the correlation function in 100 bins logarithmically spaced in separation θ to avoid bin width artefacts. For the cosmological parameter constraints, we project these on to the COSEBI basis (Schneider, Eifler & Krause 2010) to avoid the instabilities of inverting a large covariance matrix estimated via Monte Carlo simulations (we will describe our implementation of the COSEBIs in Section 4.3). However, for display purposes, it is more convenient to reduce the θ resolution to only 10 bins so that the real trends are more visually apparent.

4.1.1 Weighting

The correlation functions used here are weighted by the inverse variance of the ellipticities, where the ‘variance’ includes shape noise. Specifically, we define a weight for a galaxy

$$w_i = \frac{1}{\sigma_e^2 + 0.37^2}, \quad (22)$$

where σ_e is the ellipticity uncertainty per component defined by our shape measurement pipeline. As demonstrated by Reyes et al. (2012), these may be significantly underestimated in certain circumstances; however, this will only make our estimator slightly

suboptimal, so we do not attempt to correct for it. The value of 0.37 for the rms intrinsic ellipticity dispersion per component comes from the results of Reyes et al. (2012), for $r < 22$, and therefore we are implicitly extrapolating it to fainter magnitudes. Given that Leauthaud et al. (2007) found a constant rms ellipticity to far fainter magnitudes in the COSMOS data, we consider this extrapolation justified.¹⁹

4.1.2 Direct pair-count code

A direct pair-count correlation function code was used for the cosmological analysis. It is slow (~ 3 h for 2×10^6 galaxies on a modern laptop) but robust and well adapted to the Stripe 82 survey geometry. The code sorts the galaxies in order of increasing RA α ; the galaxies are assigned to the range $-60^\circ < \alpha < +60^\circ$ to avoid unphysical edge effects near $\alpha = 0$. It then loops over all pairs with $|\alpha_1 - \alpha_2| < \theta_{\max}$. The usual ellipticity correlation functions can be computed, e.g.

$$\xi_{++}(\theta) = \frac{\sum_{ij} w_i w_j e_{i+} e_{j+}}{\sum_{ij} w_i w_j}, \quad (23)$$

where the sum is over pairs with separations in the relevant θ bin, and the ellipticity components are rotated to the line connecting the galaxies. The direct pair-count code works on a flat sky, i.e. equatorial coordinates (α, δ) are approximated as Cartesian coordinates. This is appropriate in the range considered, $|\delta| < 1.274$, where the maximum distance distortions are $\frac{1}{2}\delta_{\max}^2 = 2.5 \times 10^{-4}$. The direct pair-count code is applicable to either autocorrelations of galaxy shapes measured in a single filter (rr , ii) or crosscorrelations between filters or between distinct populations of objects (ri and all of the star–galaxy correlations).

Simple post-processing allows one to compute the ξ_+ and ξ_- correlation functions, defined by

$$\xi_+(\theta) \equiv \xi_{++}(\theta) + \xi_{\times\times}(\theta) \quad (24)$$

and

$$\xi_-(\theta) \equiv \xi_{++}(\theta) - \xi_{\times\times}(\theta). \quad (25)$$

4.1.3 Combining bands

Finally, the different band correlation functions rr , ri , and ii must be combined according to some weighting scheme:

$$\xi_{++}^{ww}(\theta) = w_{rr}\xi_{++}^{rr}(\theta) + w_{ri}\xi_{++}^{ri}(\theta) + w_{ii}\xi_{++}^{ii}(\theta), \quad (26)$$

where the label ‘ ww ’ indicates that the bands were combined. The relative weights were chosen according to the fraction of measured shapes in r and i bands, i.e. $w_{rr} = f_r^2$, $w_{ri} = 2f_r f_i$, and $w_{ii} = f_i^2$ where the weights are $f_r = 0.4603$ and $f_i = 0.5397$.

The final ellipticity correlation functions (with the θ resolution reduced to 10 bins) are shown in Fig. 9.

¹⁹ Note that we do not use the actual value of rms ellipticity from Leauthaud et al. (2007) – only the trend with magnitude – because, as demonstrated by Mandelbaum et al. (2012), the rms ellipticity value in Leauthaud et al. (2007) is not valid for our adaptively defined moments, which use an elliptical weight function matched to the galaxy light profile.

4.2 Tests of the correlation function

We implement several null tests on the correlation function to search for remaining systematic errors.

The first test, shown in Fig. 10, constructs the difference between the cross-correlation function of r - and i -band galaxy ellipticities versus the rr and ii autocorrelations. The differences in the two types of correlation functions are small compared to the statistical uncertainty in the signal. This is consistent with our expectations, as the true cosmic shear signal should be independent of the filters in which galaxy shapes are measured.

The second test, shown in Fig. 11, compares the (band averaged or ww) correlation function computed using galaxy pairs separated in the cross-scan (north–south) direction versus pairs separated in the along-scan (east–west) direction. This difference should be zero if the signal we measure is due to lensing in a statistically isotropic universe. The error bars shown are Poisson errors, so they may be slight underestimates at the larger scales, where cosmic variance becomes important. Visual inspection shows no obvious offset from zero, but the error bars are larger for this test than in Fig. 10 because the null test includes no cancellation of galaxy shape noise.

4.3 E/B-mode decomposition

As a final check for systematics, we decompose the 2PCF into E and B modes, where, to leading order, gravitational lensing only creates E modes. The B modes can arise from the limited validity of the Born approximation (Jain, Seljak & White 2000; Hilbert et al. 2009), redshift source clustering (Schneider et al. 2002), and lensing (magnification) bias (Schmidt et al. 2009; Krause & Hirata 2010); however, the amplitude of B modes from these sources should be undetectable with our data. At our level of significance, a B-mode detection would indicate remaining systematics, e.g. due to spurious power from an incomplete PSF correction.

Formerly used methods to decompose E and B modes, such as the aperture mass dispersion

$$\langle M_{\text{ap}}^2 \rangle(\theta) = \int_0^{2\theta} \frac{d\vartheta}{2\theta^2} \left[\xi_+(\vartheta) T_+ \left(\frac{\vartheta}{\theta} \right) + \xi_-(\vartheta) T_- \left(\frac{\vartheta}{\theta} \right) \right], \quad (27)$$

with the filter functions T_{\pm} as derived in Schneider et al. (2002), or the shear E-mode correlation function, suffer from E–/B-mode mixing (Kilbinger, Schneider & Eifler 2006), i.e. B modes affect the E-mode signal and vice versa. These statistics can be obtained from the measured 2PCF, for an exact E–/B-mode decomposition; however, they require information on scales outside the interval $[\theta_{\min}; \theta_{\max}]$ for which the 2PCF has been measured.

The ring statistics (Schneider & Kilbinger 2007; Eifler, Schneider & Krause 2010; Fu & Kilbinger 2010) and more recently the COSEBIs (Schneider et al. 2010) perform an EB-mode decomposition using a 2PCF measured over a finite angular range. The COSEBIs and ring statistics can be expressed as integrals over the 2PCF as

$$EB = \int_{\theta_{\min}}^{\theta_{\max}} \frac{d\theta}{2} \theta [T_{+n}^{\log}(\theta)\xi_+(\theta) \pm T_{-n}^{\log}(\theta)\xi_-(\theta)] \quad (28)$$

and

$$R_{\text{EB}}(\theta) = \int_{\theta_{\min}}^{\theta} \frac{d\theta'}{2\theta'} [\xi_+(\theta')Z_+(\theta', \theta) \pm \xi_-(\theta')Z_-(\theta', \theta)]. \quad (29)$$

For the ring statistics, we use the filter functions Z_{\pm} specified in Eifler et al. (2010). The derivation of the COSEBI filter functions

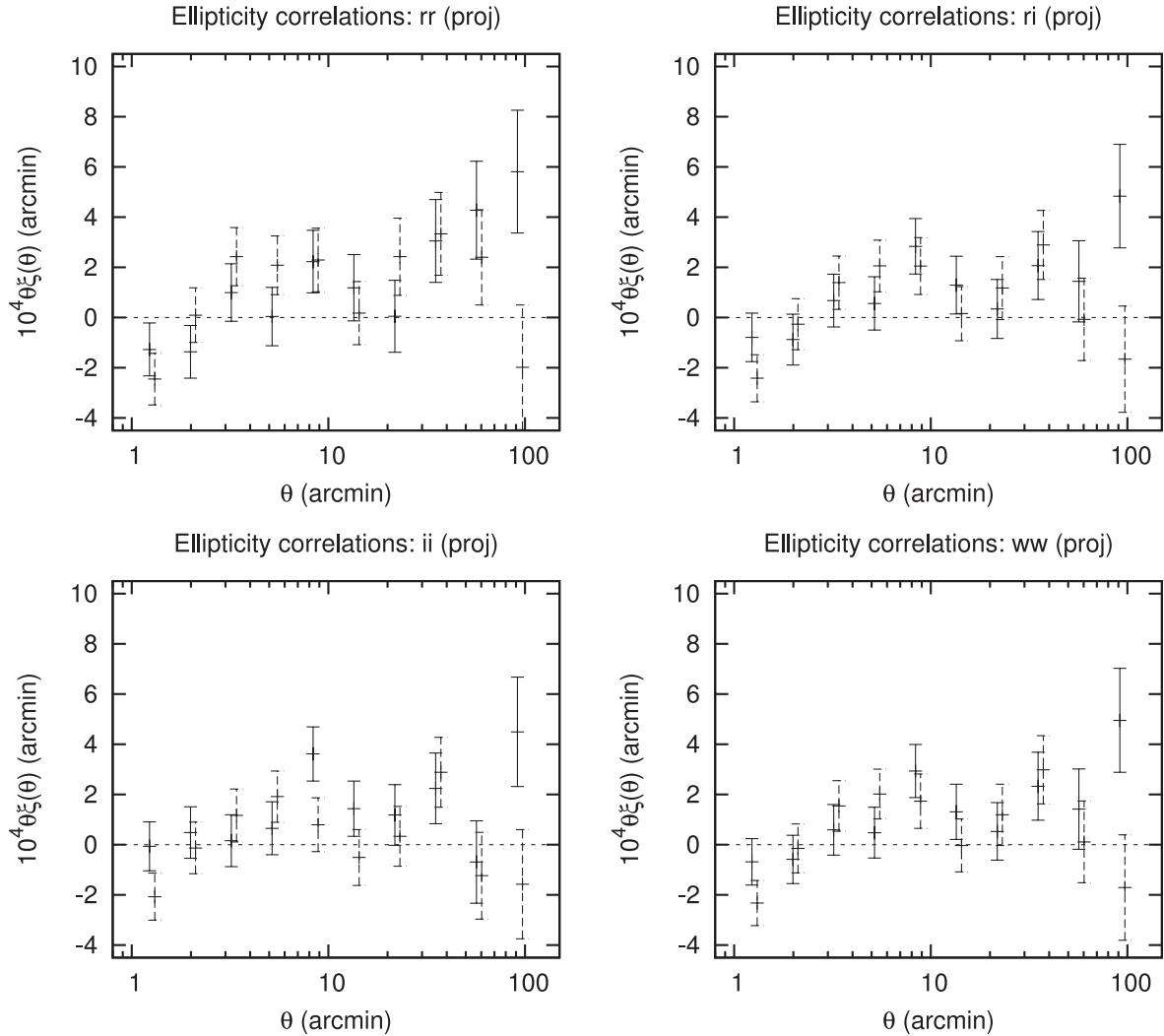


Figure 9. The ellipticity correlation functions in the *rr*, *ri*, *ii*, and *ww* (combined) band combinations. The solid points denote the ++ and the dashed points denote the ×× components of the correlation function. The points have been slightly displaced horizontally for clarity. The Monte Carlo errors are shown.

$T_{\pm n}$ is outlined in Schneider et al. (2010), where the authors provide linear and logarithmic filter functions indicating whether the separation of the roots of the filter function is distributed linearly or logarithmically in θ . Note that whereas the ring statistics are a function of angular scale, the COSEBIs are calculated over the total angular range of the 2PCF, condensing the information from the 2PCF naturally into a set of discrete modes. The linear T functions can be expressed conveniently as Legendre polynomials; however, $T_{\pm n}^{\log}$ compresses the cosmological information into significantly fewer modes; we therefore choose the logarithmic COSEBIs as our second-order shear statistic in the likelihood analysis in Section 6. The COSEBI filter functions are displayed graphically in Fig. 12.

Fig. 13 shows three different E−/B-mode statistics derived from our measured shear–shear correlation function, i.e. the COSEBIs, the ring statistics, and the aperture mass dispersion. The error bars are obtained from the square root of the corresponding covariances’ diagonal elements (statistics only). Note that the COSEBIs data points are significantly correlated. Slightly smaller is the correlation for the aperture mass dispersion, and the ring statistics’ data points have the smallest correlation.

From the COSEBIs, we find a reduced χ^2 for the E modes to be consistent with zero of 6.395, versus 1.096 for the B modes

(5 degrees of freedom each). The latter is consistent with purely statistical fluctuations.

5 COVARIANCE ESTIMATION

5.1 Ellipticity correlation function covariance matrix

The covariance matrix of the ellipticity correlation function estimated via equation (26) was computed in several ways. The preferred method for our analysis is a Monte Carlo method (Section 5.1.2) but we compare that covariance matrix with an estimate of the Poisson errors (Section 5.1.1) as a consistency check.

5.1.1 Poisson method

The direct pair-count correlation function code can compute the Poisson error bars, i.e. the error bars neglecting the correlations in $\mathbf{e}_{i+}\mathbf{e}_{j+}$ between different pairs. This estimate of the error bar is

$$\sigma^2[\xi_{++}(\theta)] = \frac{\sum_{ij} w_i^2 w_j^2 |\mathbf{e}_i|^2 |\mathbf{e}_j|^2}{2 \left[\sum_{ij} w_i w_j \right]^2}. \quad (30)$$

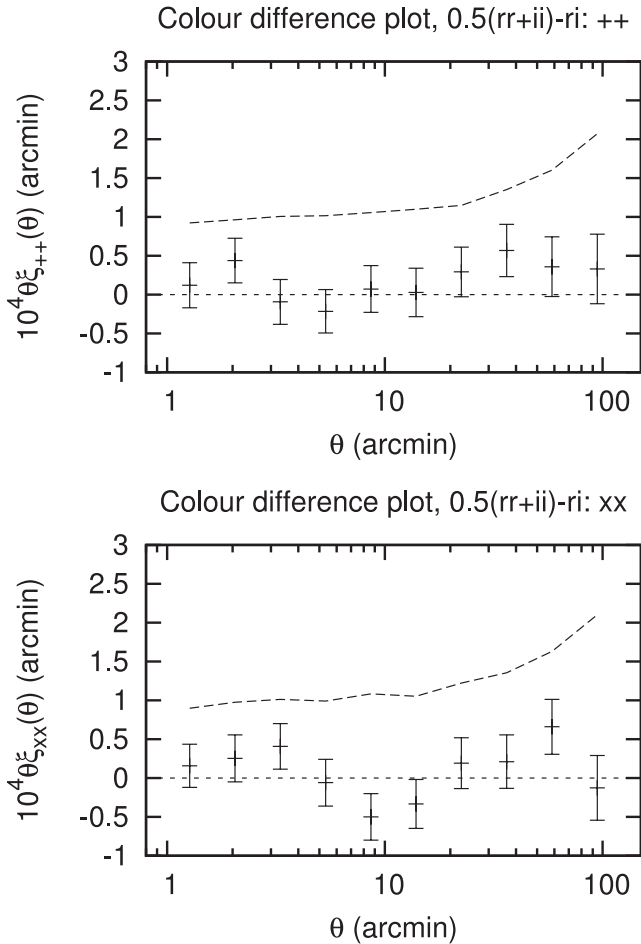


Figure 10. The difference between the galaxy ellipticity cross-correlations (ri) and the autocorrelations $(rr + ii)/2$, with error bars determined from the Monte Carlo simulations. The upper panel shows the $++$ correlations and the lower panel shows the xx correlations. The dashed line is the 1σ statistical error bar on the actual signal.

Equivalently, this is the variance in the correlation function that one would estimate if one randomly re-oriented all of the galaxies. The Poisson method is simple, however, it is not fully appropriate for ri cross-correlations (since the same intrinsic shape noise is recovered twice for pairs that appear in both ri and ir cross-correlations). Moreover, at scales of tens of arcminutes and greater there is an additional contribution because the cosmic shear itself is correlated between pairs. Therefore, the Poisson error bars should be used only as a visual guide: they would underestimate the true uncertainties if used in a cosmological parameter analysis.

5.1.2 Monte Carlo method

We used a Monte Carlo method to compute the covariance matrix of $\xi_{++}(\theta)$ and $\xi_{xx}(\theta)$. The method is part theoretical and part empirical: it is based on a theoretical shear power spectrum, but randomizes the real galaxies to correctly treat the noise properties of the survey. The advantages of the Monte Carlo method – as implemented here – are that spatially variable noise, intrinsic shape noise including correlations between the r and i band, and the survey window function are correctly represented. The principal disadvantages are that the cosmic shear field is treated as Gaussian and a particular cosmology must be assumed (see Eifler, Schneider

& Hartlap 2009, for alternative approaches). However, so long as this cosmology is not too far from the correct one (an assumption that can itself be tested!), the Monte Carlo approach is likely to yield the best covariance matrix.

The Monte Carlo approach begins with the generation of a suite of 459 realizations of a cosmic shear field in harmonic space according to a theoretical spectrum. For our analysis, the theoretical spectrum was that from the *WMAP* 7-year (Larson et al. 2011) cosmological parameter set (flat Λ CDM; $\Omega_b h^2 = 0.02258$; $\Omega_m h^2 = 0.1334$; $n_s = 0.963$; $H_0 = 71.0 \text{ km s}^{-1} \text{ Mpc}^{-1}$; and $\sigma_8 = 0.801$), and the shear power spectrum code used in Albrecht et al. (2009), itself based on the Eisenstein & Hu (1998) transfer function and the Smith et al. (2003) non-linear mapping. The redshift distribution discussed in Section 3.4.1, based on a calibration sample from DEEP2, VVDS, and PRIMUS, was used as the input to the shear power spectrum calculation.

From this power spectrum we generate a sample set of Gaussian E-mode shear harmonic space coefficients a_{lm}^E . The full power spectrum is used at $l \leq 1500$; a smooth cutoff is applied from $1500 < l < 2000$ and no power at $l \geq 2000$ is included. This is appropriate for a covariance matrix since the power at smaller scales is shot noise dominated and cannot be recovered. (The E-mode power spectrum is $C_{1500}^{EE} = 3.6 \times 10^{-11}$, as compared to a shot noise of $\gamma_{int}^2/\bar{n} \sim 1.8 \times 10^{-9}$.) No B-mode shear is included. The particle-mesh spherical harmonic transform code of Hirata et al. (2004a) with a 6144×3072 grid ($L' = 6144$) and a 400-node interpolation kernel ($K = 10$) was used to transform these coefficients into shear components (γ_1, γ_2) at the position \hat{n}_j of each galaxy j .²⁰

A synthetic ellipticity catalogue was then generated as follows. For each galaxy, we generated a random position angle offset $\psi_j \in [0, \pi)$ and rotated the ellipticity in both r and i bands by ψ_j .²¹ We then added the synthetic shear weighted by the shear responsivity to the randomized ellipticity to generate a synthetic ellipticity

$$e_j^{\text{syn}} = e^{2i\psi_j} e_j^{\text{true}} + 1.73\gamma(\hat{n}_j). \quad (31)$$

The 1.73 pre-factor was estimated from equation (14), which we expected to be good enough for use in the Monte Carlo analysis, so that the Monte Carlos could be run in parallel with the shear calibration simulations. The latter gave a final result of 1.78 ± 0.04 , which is not significantly different.

The direct pair-count correlation function code, in all versions (rr , ri , and ii) was run on each of the 459 Monte Carlo realizations, before combining the different correlations to get the weighted value via equation (26).

The Monte Carlo and Poisson error bars are compared in Fig. 14. The correlation coefficients of the correlation functions in different bins are plotted graphically in Fig. 15.

From each Monte Carlo correlation function we compute the COSEBIs via equation (28) and use their covariance matrix in our subsequent likelihood analysis. In order to test whether our covariance has converged, meaning that the number of realizations is sufficient to not alter cosmological constraints, we perform three likelihood analyses in σ_8 versus Ω_m space varying the numbers

²⁰ The use of a full-sky approach for the Monte Carlo realizations was not necessary for the SDSS Stripe 82 project, but was the simplest choice given legacy codes available to us.

²¹ To simplify bookkeeping, the actual implementation was that a sequence of 10^7 random numbers was generated, and a galaxy was assigned to one of these numbers based on its coordinates in a fine grid with 0.36 arcsec cells in (α, δ) .

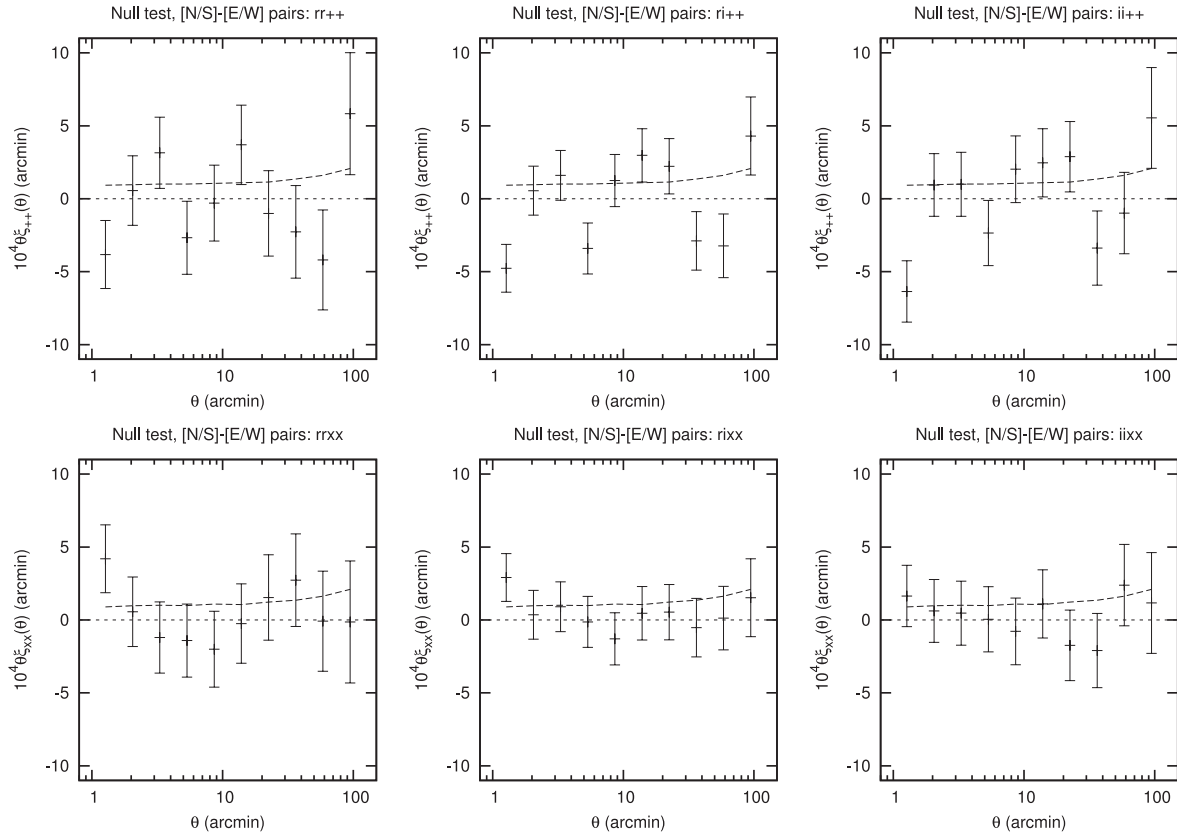


Figure 11. The null test of the correlation functions measured using galaxy pairs whose separation vector is within 45° of the north–south direction, minus that measured using galaxy pairs whose separation vector is within 45° of the east–west direction. The error bars shown are the Poisson errors only. The dashed curve shows the 1σ error bars of the actual signal (all colour combinations and separation vectors averaged). The six panels show the three colour combinations (*rr*, *ri*, and *ii*) and the two components (+ + or $\times \times$).

of realizations from which we compute the covariance matrix (see Section 6 for detailed methodology; for now we are just establishing convergence of the covariance matrix). In Fig. 16 we show the 68 and 95 per cent likelihood contours, i.e. the contours enclose the corresponding fraction of the posterior probability (within the ranges of the parameters shown). We see that the contours hardly change when going from 300 to 400 realizations and show no change at all when going from 400 to 459 realizations, hence the 459 Monte Carlo realizations are sufficient for our likelihood analysis.

5.2 Systematic contributions to the covariance matrix

The following additional contributions are added to the Monte Carlo covariance matrix (and if appropriate the theory result) described in Section 5.1.2.

(i) The intrinsic alignment error was included following Section 3.2: the theory shear correlation function was reduced by a factor of 0.92, and an uncertainty of 4 per cent of the theory was added to the covariance matrix, i.e. we add an intrinsic alignment contribution

$$\text{Cov}[\xi_i, \xi_j](\text{intrinsic alignment}) = 0.04^2 \xi_i^{(\text{th})} \xi_j^{(\text{th})}, \quad (32)$$

where the theory curve (th) is obtained at the fiducial *WMAP7* point. This covariance matrix includes perfect correlation between radial bins, implying that we treat this systematic as being an effect with a fixed scaling with separation, so the only degree of freedom is its amplitude.

(ii) The stellar contamination was included following Section 3.5: the theory shear correlation function was reduced by a factor of 0.936, and an uncertainty of 3 per cent of the theory was added to the covariance matrix, i.e. we add a stellar contamination contribution

$$\text{Cov}[\xi_i, \xi_j](\text{stellar contamination}) = 0.03^2 \xi_i^{(\text{th})} \xi_j^{(\text{th})}, \quad (33)$$

where the theory curve (th) is obtained at the fiducial *WMAP7* point.

(iii) The implied error from the redshift distribution uncertainty is derived from 402 realizations of the sampling variance simulations as described in Section 3.4.2. We construct the covariance matrix of the predicted E-mode COSEBIs.

(iv) The shear calibration uncertainty was conservatively estimated in Section 3.3 to be ± 2.4 per cent, or equivalently 4.8 per cent in second-order statistics. We thus add another term to the covariance matrix,

$$\text{Cov}[\xi_i, \xi_j](\text{shear calibration}) = 0.048^2 \xi_i^{(\text{th})} \xi_j^{(\text{th})}. \quad (34)$$

(v) In Section 3.6, we described a procedure for including uncertainty due to additive PSF contamination. According to this procedure, the relevant systematics covariance matrix is related to the amplitude of the measured contamination signal

$$\text{Cov}[\xi_i, \xi_j](\text{PSF contamination}) = 0.9^2 \xi_{\text{sg},i} \xi_{\text{sg},j}, \quad (35)$$

again assuming a fixed scaling with radius for this systematic uncertainty. Since all entries scale together, we do not spuriously ‘average down’ our estimate of the systematic error by combining many bins.

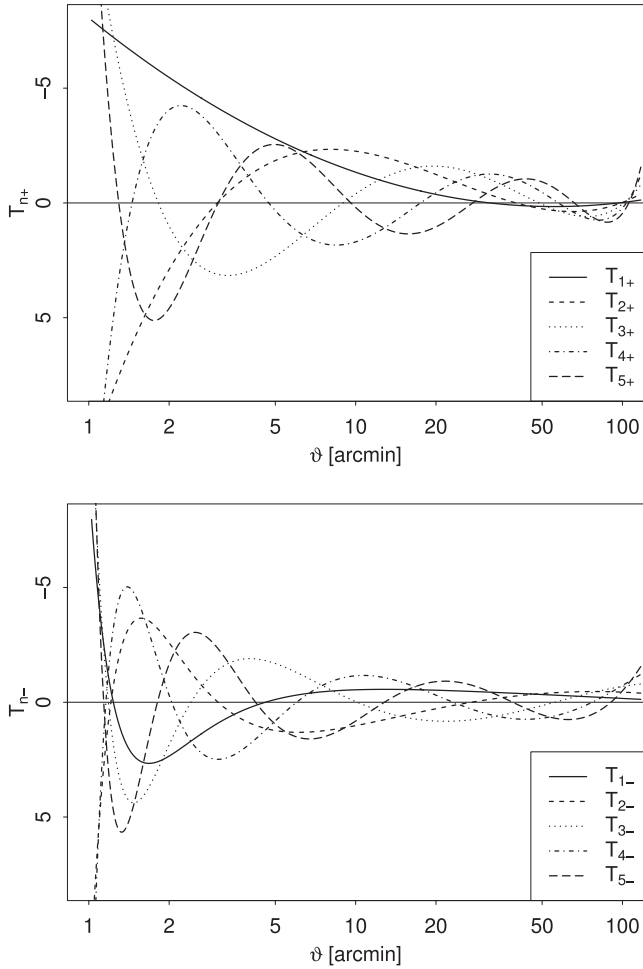


Figure 12. The COSEBI filter functions T_{n+} (upper panel) and T_{n-} (lower panel) for the first five modes.

The final data vector and its covariance matrix (including all the statistical and systematic components) are given in Tables A1 and A2. Note that given our procedure of applying the systematic corrections to the theory, the data vector is the observed one without any such corrections for the stellar contamination and intrinsic alignments contamination. With this in hand, we can estimate the

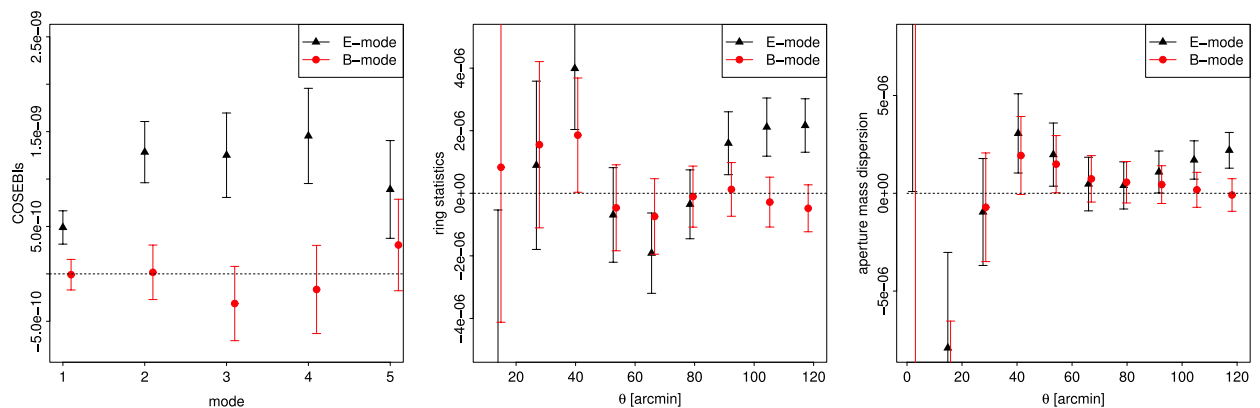


Figure 13. The measured COSEBIs, ring statistics, and aperture mass dispersion from the combined cosmic shear signal. The error bars equal the square root of the corresponding covariances' diagonal elements (statistics only). Note that the COSEBIs data points are significantly correlated. Slightly smaller is the correlation for the aperture mass dispersion, and the ring statistics' data points have the smallest correlation.

significance of the E- and B-mode signals described in Section 4.3. The probability that the COSEBI E-mode signal that we observe is due to random chance given the null hypothesis (no cosmic shear) is 6.0×10^{-6} . The probability of measuring our B-mode signal due to random chance given the null hypothesis of zero B modes is 0.36, evidence that there is no significant B-mode power.

6 COSMOLOGICAL CONSTRAINTS

Having described the measured cosmic shear two-point statistics, and shown that the systematic bias in this measurement is small compared with the statistical constraints, we now turn to the cosmological interpretation. We work in the context of the flat Λ CDM parametrization, taking where necessary the *WMAP7* (Komatsu et al. 2011) constraints for our fiducial parameter values.

6.1 The prediction code: modelling second-order shear statistics

To produce a cosmological interpretation of our measured cosmic shear signal from our model framework, we require a method to convert a vector of cosmological parameters into a prediction of the observed cosmic shear signal. Due to projection effects, we expect that a significant fraction of the observed cosmic shear signal is produced by the clustering of matter on non-linear scales, so a suitably accurate prediction algorithm must ultimately rely on numerical simulations of structure formation.

The prediction code used in our likelihood analysis is a modified version of the code described in Eifler (2011). We combine Halofit (Smith et al. 2003), an analytic approach to modelling non-linear structure, with the Coyote Universe Emulator (Lawrence et al. 2010), which interpolates the results of a large suite of high-resolution cosmological simulations over a limited parameter space, to obtain the density power spectrum. The derivation is a two-step process: first, we calculate the linear power spectrum from an initial power-law spectrum $P_\delta(k) \propto k^{n_s}$ employing the dewiggled transfer function of Eisenstein & Hu (1998). The non-linear evolution of the density field is incorporated using Halofit. In order to simulate w CDM models we follow the scheme implemented in *ICOSMO* (Refregier et al. 2011), interpolating between flat and open cosmological models to mimic Quintessence cosmologies (see Schrabback et al. 2010 for more details). In a second step, we match the Halofit power spectrum to the Coyote Universe Emulator (version

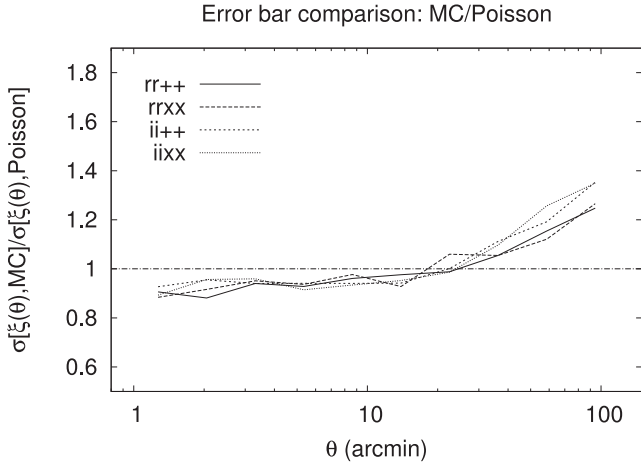


Figure 14. The ratio of error bars obtained by the Monte Carlo method to those obtained by the Poisson method, for 10 angular bins. The four curves show either rr or ii band correlation functions, and either the $++$ or $\times\times$ component. Note the rise in the error bars at large values of the angular separation, due to mode sampling variance.

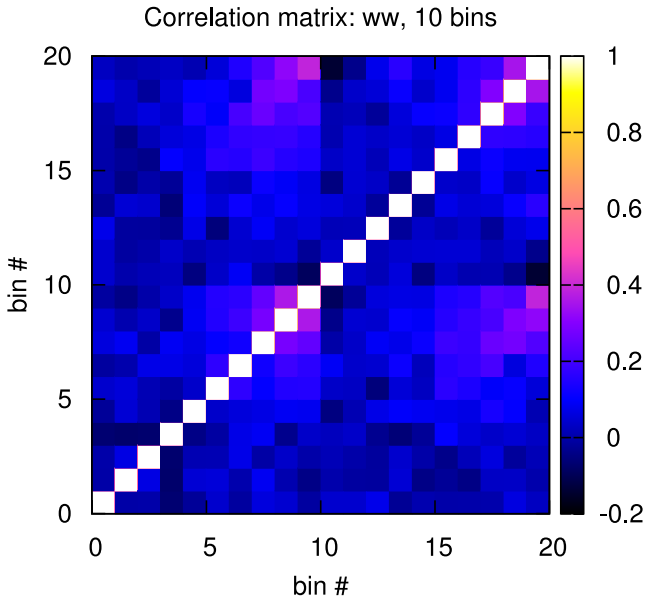


Figure 15. The matrix of correlation coefficients for the combined (ww) correlation functions in the 10 angular bins for which the correlation function is plotted in the companion figures. The bin number ranges from 0 to 9 for $\xi_{++}(\theta)$ and from 10 to 19 for $\xi_{\times\times}(\theta)$; all diagonal components are by definition equal to unity. Based on 459 Monte Carlo realizations.

1.1) power spectrum, which emulates P_δ over the range $0.002 \leq k \leq 3.4 h \text{ Mpc}^{-1}$ within $0 \leq z \leq 1$ to an accuracy of 1 per cent. Wherever possible, the matched power spectrum exactly corresponds to the Coyote Universe Emulator; of course this is limited by the cosmological parameter space of the Emulator and its limited range in k and z . However, even outside the range of the Emulator, we rescale the Halofit power spectrum with a scalefactor $P_\delta(\text{Coyote})/P_\delta(\text{Halofit})$ calculated at the closest point in parameter space (cosmological parameters, k , and z) where the Emulator gives results. Outside the range of the Emulator, the accuracy of this ‘Hybrid’ density power spectrum is of course worse than 1 per cent; however, it should be a significant improvement over a density power spectrum from Halofit only. From the so-derived density power spectrum we calcu-

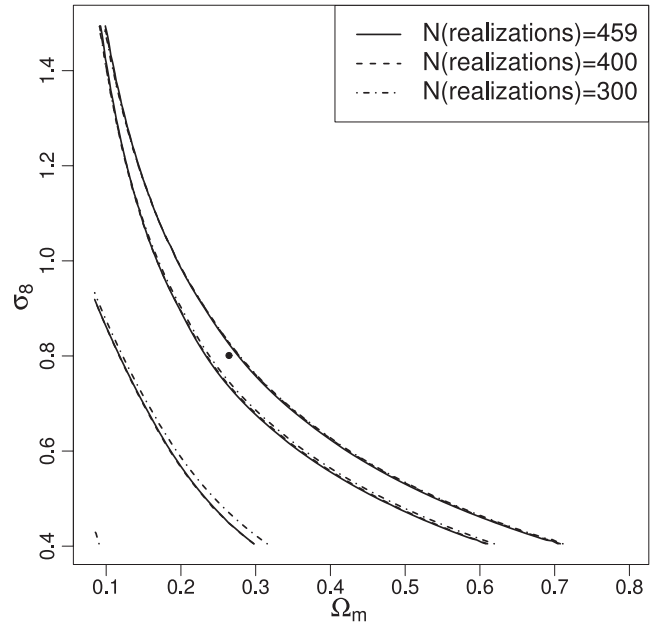


Figure 16. Convergence test of the σ_8 versus Ω_m parameter constraints as a function of the number of Monte Carlo realizations used to compute the covariance. The plot shows the 68 and 95 per cent likelihood contours (however, the lower 95 per cent contours are not visible). The covariance includes statistical errors only.

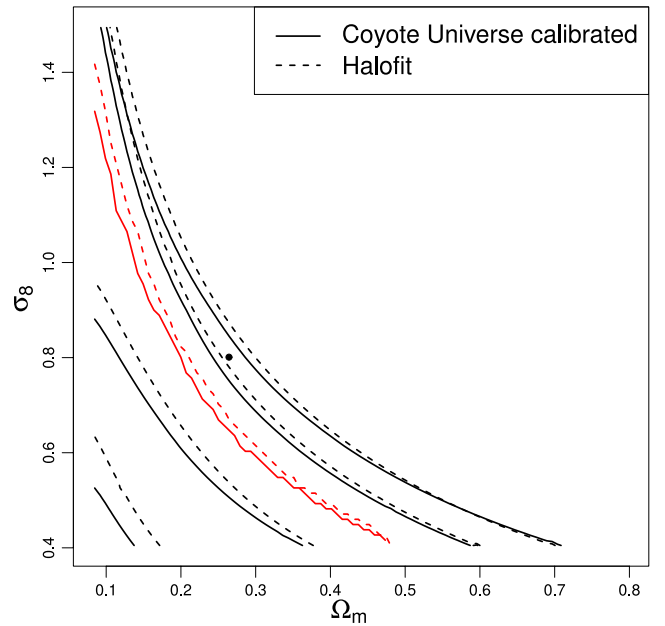


Figure 17. The 68 and 95 per cent likelihood contours of the combined data vector including a full treatment of systematics when using the Halofit prediction code (dashed) and when using the Coyote Universe-calibrated prediction code (solid). The red lines correspond to the best-fitting value of σ_8 for a given Ω_m . The dot indicates the *WMAP7* best-fitting values.

late the shear power spectrum via equation (11) and the shear–shear correlation function via equation (10). As a final step, we transform these predicted correlation functions to the COSEBI basis as described above in Section 4.3.

For our final results in the (Ω_m, σ_8) likelihood analysis, we used both prediction codes; the results are compared in Fig. 17,

where they are seen to agree to much better than 1σ . We therefore conclude that uncertainty in the theory predictions is subdominant to the other sources of systematic error, and to the statistical error.

6.2 Constructing the input data vector

For our primary science results, we use the measured five COSEBI modes (see Fig. 13, left-hand panel). As a first step we want to determine the number of COSEBI modes that need to be included in our likelihood analysis. In Fig. 18 we show a likelihood analysis in the σ_8 – Ω_m parameter space varying the number of modes in the data vector. We find that there is hardly a change in the likelihood contours when going from four to five modes; we therefore conclude that five modes is a sufficient number to capture the cosmological information encoded in our data set.

As shown in Eifler, Kilbinger & Schneider (2008), the information content of the aperture mass dispersion can be greatly improved when including 1 data point of the shear–shear correlation function ξ_+ into the data vector; here we adopt this concept for the COSEBIs. The basic idea is that the data point of the correlation function is sensitive to scales of the power spectrum to which the COSEBIs are insensitive. We incorporate only a single data point of the correlation function as this is sufficient to capture the bulk of the additional information while simultaneously minimizing possible B-mode contamination.

In order to determine the optimal scale of the data point that is to be included, we consider 10 bins of ξ_+ ranging from 1.3 to 97.5 arcmin and perform 10 likelihood analyses for a combined data vector consisting of five COSEBI modes and one additional data point of ξ_+ . We quantify the information content through the

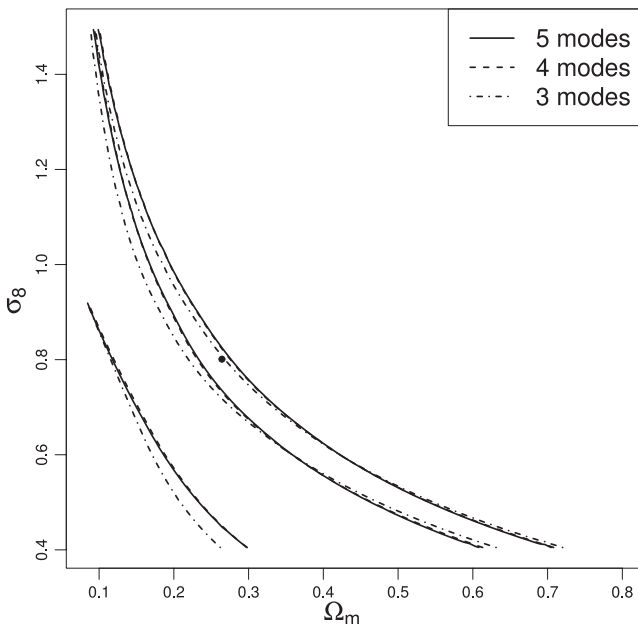


Figure 18. Convergence test of the σ_8 versus Ω_m parameter constraints as a function of number of the COSEBI modes in the data vector. The plot shows the likelihood contours enclosing 68 and 95 per cent of the posterior distribution. (The lower bounding curve for the 95 per cent contours is not visible on the plot.) The covariance contains statistical errors only. The dot indicates the *WMAP7* best-fitting values.

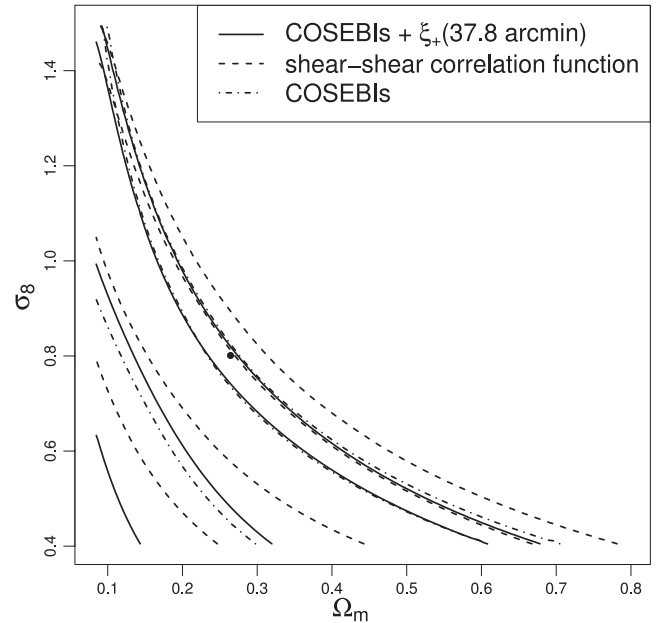


Figure 19. The likelihood contours of the combined data vector (solid), the shear–shear correlation function (dashed), and the COSEBIs (dotted) data vector to illustrate how much information is gained when including the additional data point. Note that the COSEBIs’ lower 95 per cent contour is outside the considered region. The dot indicates the *WMAP7* best-fitting values.

so-called q figure of merit (q -FoM)

$$q = \sqrt{|\mathbf{Q}|}, \text{ where}$$

$$\mathbf{Q}_{ij} = \int d^2\pi p(\pi|\mathbf{d}) (\pi_i - \pi_i^f) (\pi_j - \pi_j^f), \quad (36)$$

$\pi = (\Omega_m, \sigma_8)$ is the parameter vector, $p(\pi|\mathbf{d})$ is the posterior likelihood at this parameter point, and π_i^f denotes the fiducial parameter values. If the likelihood in parameter space (i.e. the posterior probability) is Gaussian, the q -FoM corresponds to the more common Fisher matrix based figure of merit $f = 1/|\sqrt{\mathbf{F}}|$. The Fisher matrix \mathbf{F} can be interpreted as the expectation value of the inverse parameter covariance evaluated at the maximum likelihood estimate parameter set, which in our ansatz corresponds to the fiducial parameters. Mathematically we can express this equivalence as

$$f = \frac{1}{\sqrt{|\mathbf{F}|}} = \sqrt{|\mathbf{C}_\pi|} = \sqrt{|\mathbf{Q}|} = q. \quad (37)$$

Since the assumption of a Gaussian posterior is clearly violated in the σ_8 – Ω_m parameter space, we perform a full likelihood analysis and calculate q to quantify the size of the likelihood. Note that smaller q -FoM is ‘better.’

We varied the angular scale (in arcmin) of the added $\xi_+(\theta)$ data point, and found a minimal q -FoM at $\theta = 37.8$ arcmin. We will use this scale for the additional ξ_+ data point henceforth. Note that this analysis uses a simulated input data vector in order to avoid biases from designing a statistical test based on the observed data. The constraints coming from the various possible data vectors – the COSEBIs, the COSEBIs supplemented with a single ξ_+ point, and the full shear correlation function – are compared in Fig. 19. They are not identical, which is expected since they weight the data in different ways, but are consistent with each other.

The COSEBI modes are highly correlated with each other, and they are correlated to a lesser extent with ξ_+ at 38 arcmin. The

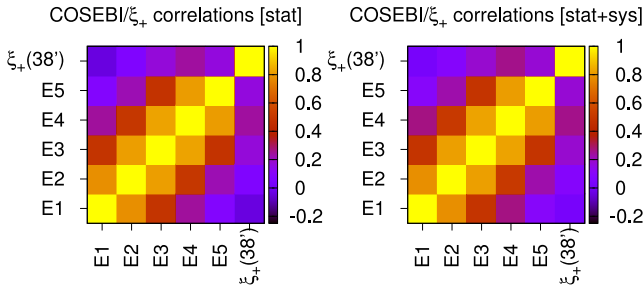


Figure 20. The correlation matrix of the COSEBI modes 1–5 (‘E1...E5’ in the figure) and $\xi_+(38')$. The left-hand panel shows only the statistical (Monte Carlo) errors, and the right-hand panel includes the systematics as well.

correlation matrix is shown in Fig. 20, and the corresponding covariance matrix is tabulated in the appendix in Table A2.

6.3 Parameter fits

We perform all of our fits to a standard five-parameter Λ CDM model.²² For the initial likelihood analysis, we fix n_s , $\Omega_b h^2$, $\Omega_m h^2$, and w_0 at their fiducial best-fitting *WMAP7* values (Komatsu et al. 2011), and vary σ_8 . The upper panel of Fig. 21 shows the likelihood of σ_8 with all other parameters fixed, with a value at the peak and 68 per cent confidence interval of $0.636^{+0.109}_{-0.154}$. For a survey of this size and depth, the constraints are comparable to the statistically achievable confidence limits.

We also perform a likelihood analysis fixing three parameters, and varying Ω_m and σ_8 simultaneously, as these two parameters are much more sensitive to the measured cosmic shear signal than the others. The resulting 2D constraints are shown in the bottom panel of Fig. 21. Our 68 per cent confidence limits on the degenerate product $\sigma_8 \left(\frac{\Omega_m}{0.264}\right)^{0.67}$ are $0.65^{+0.12}_{-0.15}$ for the Coyote Universe prediction code (see Fig. 21, solid red line), and $\sigma_8 \left(\frac{\Omega_m}{0.264}\right)^{0.72} = 0.67^{+0.12}_{-0.15}$ for the Halofit prediction code (see Fig. 21, dashed red line).

We show the effects of removing each systematic error correction, Fig. 21 also shows, for both the 1D and 2D analyses, the impact of systematic error corrections. The combined effects of these uncertainties are clearly substantially smaller than the statistical error on the amplitude of the shear signal.

Finally, we adopt the *WMAP7* likelihoods as priors, and evaluate our likelihood at each link in the *WMAP7* Markov chain. For each chain element, we assign a weight equal to our likelihood function evaluated at the parameter vector for that chain element. For each of the parameter constraint plots shown here, we first assign each Markov chain Monte Carlo (MCMC) chain element to a point on a regular grid in the parameter space; the value of the marginalized likelihood at each grid point, $H_{i,j}$ is then the sum of our likelihood weights over the MCMC chain elements at the (i,j) grid point,

$$H_{i,j} = \sum_k I_k(i,j) L_k, \quad (38)$$

where the indicator function $I_k(i,j)$ is equal to unity when the (i,j) grid point in parameter space is nearest the k th chain element,

²² The optical depth to reionization τ is a sixth parameter implicitly included in the *WMAP7* chains, but with no effect on the lensing shear correlation function.

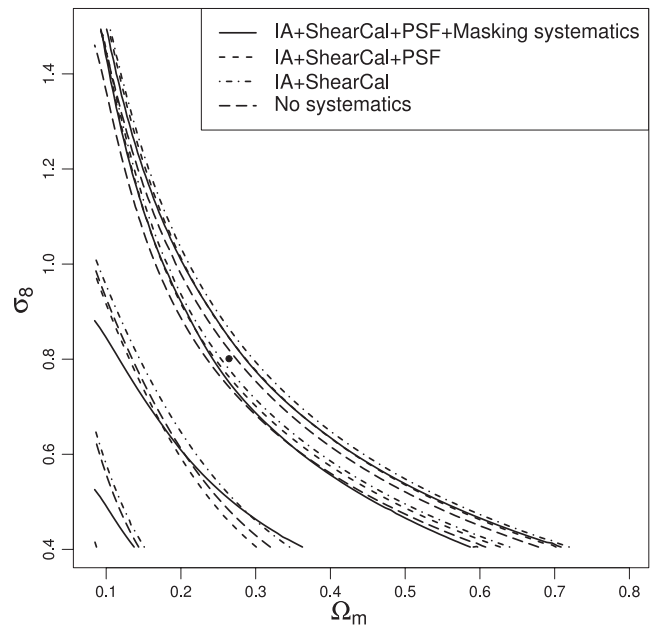
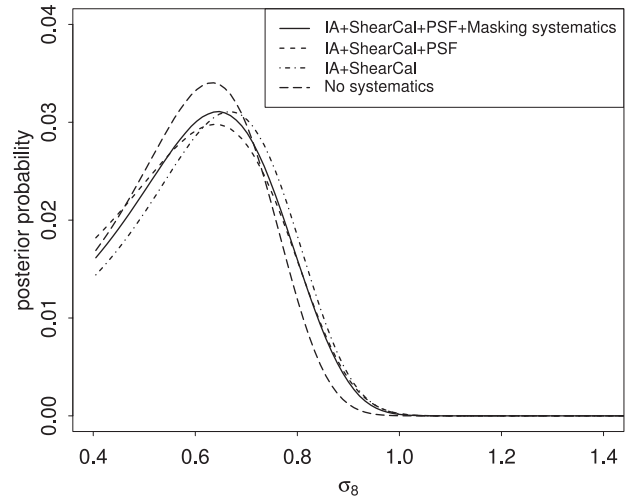


Figure 21. The effect of systematic errors in the 1D likelihood of σ_8 (upper panel) and in the 2D constraints (68 per cent likelihood contours only) in the σ_8 - Ω_m plane (lower panel). The solid curve shows our final analysis, while the other curves show results including subsets of the systematic errors. The dot-dashed curve labelled ‘no systematics’ shows only the statistical errors, without any systematic error corrections either to the theory or to the covariance matrix. The dot indicates the *WMAP7* best-fitting values.

and zero otherwise. The likelihood L_k for each chain element is evaluated in the usual way as

$$L_k = \exp\left(-\frac{\vec{d}_k^T \mathbf{C}^{-1} \vec{d}_k}{2}\right). \quad (39)$$

Here \mathbf{C} is the full covariance matrix for the measurement, incorporating both the statistical and systematic uncertainties, and the normalization is arbitrary. The data vector \vec{d}_k is the extended COSEBI vector described above; where shown, the *WMAP7* priors are simply this sum with $L_k = 1$ for each point.

We estimate the detection significance for the final signal, the difference $\sqrt{-2\Delta \log L}$ between the highest likelihood Markov chain element for both the Λ CDM and w CDM models and the

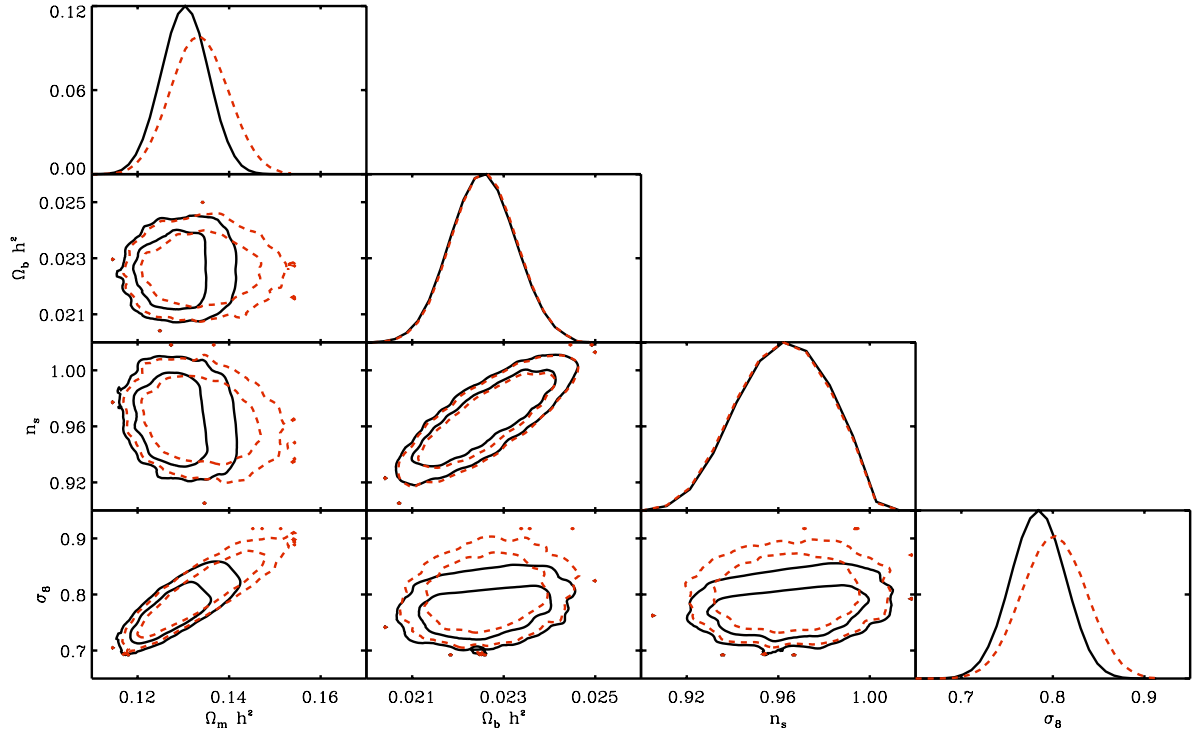


Figure 22. The cosmological parameter constraints using the extended COSEBI data vector, fixing the dark energy equation of state w at -1 , but allowing all other parameters to vary. Off-diagonal panels show joint 2D constraints after marginalization over all the other parameters, which are shown. For these, the red contours show the *WMAP7* priors containing 68.5 and 95.4 per cent of the posterior probability. The black contours are the same but for *WMAP7*+SDSS lensing. Diagonal panels show the fully marginalized 1D posterior distribution for each parameter; for these panels, the red (dashed) contours show the marginalized *WMAP7* constraints.

likelihood evaluated with no signal. The 1σ detection significances for these two models are 2.64 and 2.88, respectively. This is not the significance of the detection of cosmic shear (as in Section 5.2), but rather a measurement of the likelihood of these two models given the combination of *WMAP7* priors with this experiment.

In Fig. 22, we show marginalized posterior likelihoods in the case of fixed Λ CDM (i.e. $w = -1$) for $\Omega_m h^2$, $\Omega_b h^2$, n_s , and σ_8 . The results with a free equation of state of dark energy (w CDM) are in Fig. 23. Our measurement provides some additional constraints beyond those from *WMAP7* on these parameters. In particular, the low amplitude of the measured shear signal rules out some of the previously allowed volume of $\Omega_m h^2$ and σ_8 *WMAP7* constraints.

7 CONCLUSIONS

Using co-added imaging constructed from SDSS Stripe 82 data, we constructed a weak lensing catalogue of 1328 885 galaxies covering 168 square degrees (Paper I), and showed that the additive shear systematics arising from the PSF are negligible compared to the cosmic shear signal. In this paper, we carried out a cosmic shear measurement that resulted in a 20 per cent constraint on σ_8 (with all other cosmological parameters fixed). This adds constraining power beyond that from *WMAP7*, and serves as an important independent data point on the amplitude of the matter power spectrum at late times. In particular, the primary CMB anisotropies presently provide only a modest constraint on $\Omega_m h^2$, and (due to the effect of matter density on the growth of structure) there is then an elongated allowed region in the $(\Omega_m h^2, \sigma_8)$ plane; see Fig. 22. The *WMAP7*-allowed region is ideally oriented for lensing to play a role: the lensing signal at the high- $\Omega_m h^2$, high- σ_8

end of the ellipse leads to a much higher lensing signal than low $\Omega_m h^2$, low σ_8 . The low amplitude of cosmic shear observed in this paper eliminates the high- $\Omega_m h^2$, high- σ_8 solutions, and leads to a *WMAP7*+SDSS lensing solution of $\sigma_8 = 0.784^{+0.028}_{-0.026}(1\sigma)^{+0.055}_{-0.054}(2\sigma)$ and $\Omega_m h^2 = 0.1303^{+0.0047}_{-0.0048}(1\sigma)^{+0.0091}_{-0.0092}(2\sigma)$; the 2σ error ranges are, respectively, 14 and 17 per cent smaller than for *WMAP7* alone.

We have also carefully evaluated other sources of uncertainty such as the source redshift distribution, intrinsic alignments, and shear calibration, to ensure that our measurement is dominated by statistical errors rather than systematic errors. This achievement is important when considering that (i) the SDSS data were never designed with this application in mind, and indeed includes several features (e.g. the minimal amount of cross-scan dithering) that cause significant difficulty, and (ii) with the multitude of upcoming multi-exposure lensing surveys in the next few years, it is important to cultivate new data analysis techniques (such as the one used here) that are capable of producing homogeneous data with tight control over PSF anisotropies. As a quantitative measure of the extent of PSF correction possible with SDSS data, we take the rms residual spurious shear at a particular scale estimated from the star-galaxy correlations,

$$\gamma_{\text{rms,eq}}(\theta) = \frac{\sqrt{\mathcal{R}_{\text{psf}} \xi_{+, \text{sg}}(\theta)}}{\mathcal{R}}. \quad (40)$$

From Fig. 7, we see that this is $\sim 2 \times 10^{-3}$ at the smallest scales (1–6 arcmin), is $< 10^{-3}$ at scales $\theta > 0.1$, and drops to 3.7×10^{-4} in the final bin (1.2–2.0).²³ There is almost no difference between

²³ We used $\mathcal{R}_{\text{psf}} = 0.9$ and $\mathcal{R} = 1.776$, as described in the text.

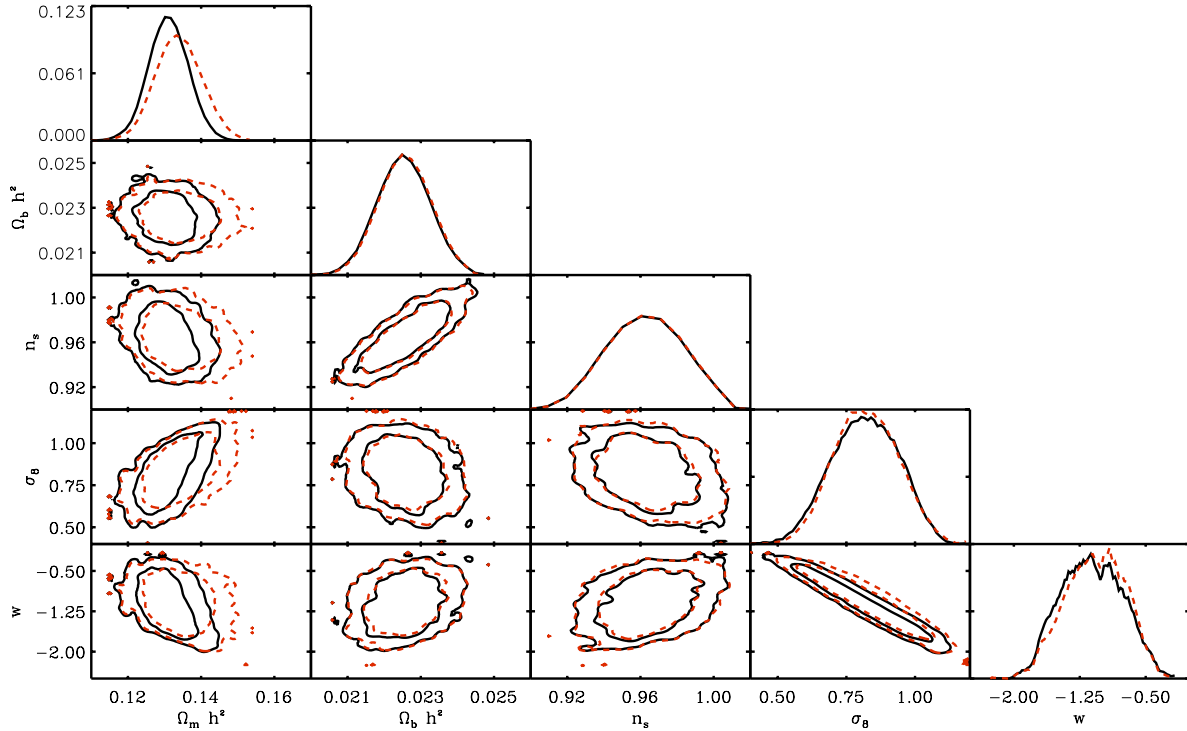


Figure 23. The cosmological parameter constraints using the extended COSEBI data vector, varying all five parameters. Off-diagonal panels show joint 2D constraints after marginalization over all the other parameters, which are shown. For these, the red contours show the *WMAP7* priors containing 68.5 and 95.4 per cent of the posterior probability. The black contours are the same but for *WMAP7*+SDSS lensing. Diagonal panels show the fully marginalized 1D posterior distribution for each parameter; for these panels, the red (dashed) contours show the marginalized *WMAP7* constraints.

the $++$ and $\times\times$ signals, suggesting that the spurious additive ellipticity signal contains similar amounts of E and B modes;²⁴ something similar was seen in the SDSS single-epoch data via run-by-run comparisons of ellipticity measurements on the same galaxies (Mandelbaum et al. 2006b, fig. 8). This is good news for the use of the B mode as a diagnostic of PSF systematics, although an understanding of the generality of this pattern remains elusive.

An important lesson learned from this project is the importance of *masking bias*, in which the intrinsic orientation of a galaxy affects whether it falls within the survey mask. This is likely the main reason why we had to implement the $\langle e_1 \rangle$ projection. While we have clearly not exhausted the range of options for removing this bias at the catalogue level, future surveys should be designed to produce more uniform data quality via an appropriate dithering strategy and suppress the masking bias at the earliest stages of the analysis.

Our major limitation in the end was the source number density, which was driven by the fact that our PSF-matching procedure was limited by the worst seeing in the images that we use, and therefore we had to eliminate the images with seeing worse than the median. This means that the co-adds were not as deep as they could have been, and the final effective seeing was 1.31 arcsec (full width at half-maximum). In principle this will be an obstacle to applying this technique in the future, but in fact, that statement depends on context. For example, for a survey such as HSC or LSST where we expect typically ~ 0.7 arcsec seeing, and with plans to preferentially use the best-seeing nights for r - and i -band imaging that will be used for shape measurement, it is conceivable that nearly all images

intended for lensing will have seeing in the 0.6–0.8 arcsec range. In that context, a PSF-matched co-add that has the rounding kernel applied may actually not result in much loss of information about the shapes of most useful galaxies, and will have the advantage of the removal of PSF anisotropies. Moreover, even for surveys for which the loss of information that results from this method may not be suitable for the final cosmological analysis, this method may still serve as a useful diagnostic of the additive PSF systematics.

ACKNOWLEDGEMENTS

We thank Alexie Leauthaud for providing faint COSMOS galaxy postage-stamp images for simulation purposes. EMH is supported by the US Department of Energy’s Office of High Energy Physics (DE-AC02-05CH11231). During the period of work on this paper, CMH was supported by the US Department of Energy’s Office of High Energy Physics (DE-FG03-02-ER40701 and DE-SC0006624), the US National Science Foundation (AST-0807337), the Alfred P. Sloan Foundation, and the David & Lucile Packard Foundation. RM was supported for part of the duration of this project by NASA through Hubble Fellowship grant #HST-HF-01199.02-A awarded by the Space Telescope Science Institute, which is operated by the Association of Universities for Research in Astronomy, Inc., for NASA, under contract NAS 5-26555. US is supported by the DOE, the Swiss National Foundation under contract 200021-116696/1 and WCU grant R32-10130.

We thank the PRIMUS team for sharing their redshift catalogue, and thank Alison Coil and John Moustakas for help with using the PRIMUS data set. Funding for PRIMUS has been provided by NSF grants AST-0607701, 0908246, 0908442, 0908354, and NASA grant 08-ADP08-0019. This paper includes data gathered with the

²⁴ Recall that $\xi_{++}(\theta) - \xi_{\times\times}(\theta)$ and $P_E(\ell) - P_B(\ell)$ are J_4 Hankel transforms of each other.

6.5 m Magellan Telescopes located at Las Campanas Observatory, Chile.

EMH thanks CCAPP for the hospitality during CCAPP Symposium and participants support provided through NSF grant #1135622.

Funding for the DEEP2 survey has been provided by NSF grants AST95-09298, AST-0071048, AST-0071198, AST-0507428, and AST-0507483 as well as NASA LTSA grant NNG04GC89G. Some of the data presented herein were obtained at the W. M. Keck Observatory, which is operated as a scientific partnership among the California Institute of Technology, the University of California and the National Aeronautics and Space Administration. The Observatory was made possible by the generous financial support of the W. M. Keck Foundation. The DEEP2 team and Keck Observatory acknowledge the very significant cultural role and reverence that the summit of Mauna Kea has always had within the indigenous Hawaiian community and appreciate the opportunity to conduct observations from this mountain.

Funding for the SDSS and SDSS-II has been provided by the Alfred P. Sloan Foundation, the Participating Institutions, the National Science Foundation, the US Department of Energy, the National Aeronautics and Space Administration, the Japanese Monbukagakusho, the Max Planck Society, and the Higher Education Funding Council for England. The SDSS website is <http://www.sdss.org/>.

The SDSS is managed by the Astrophysical Research Consortium for the Participating Institutions. The Participating Institutions are the American Museum of Natural History, Astrophysical Institute Potsdam, University of Basel, University of Cambridge, Case Western Reserve University, University of Chicago, Drexel University, Fermilab, the Institute for Advanced Study, the Japan Participation Group, Johns Hopkins University, the Joint Institute for Nuclear Astrophysics, the Kavli Institute for Particle Astrophysics and Cosmology, the Korean Scientist Group, the Chinese Academy of Sciences (LAMOST), Los Alamos National Laboratory, the Max-Planck-Institute for Astronomy (MPIA), the Max-Planck-Institute for Astrophysics (MPA), New Mexico State University, Ohio State University, University of Pittsburgh, University of Portsmouth, Princeton University, the United States Naval Observatory, and the University of Washington.

REFERENCES

- Albrecht A. et al., 2006, preprint (astro-ph/0609591)
 Albrecht A. et al., 2009, preprint (arXiv:0901.0721)
 Bacon D. J., Refregier A. R., Ellis R. S., 2000, MNRAS, 318, 625
 Benabed K., van Waerbeke L., 2004, Phys. Rev. D, 70, 123515
 Benjamin J. et al., 2007, MNRAS, 381, 702
 Bernstein G., 2010, MNRAS, 406, 2793
 Bernstein G., Huterer D., 2010, MNRAS, 401, 1399
 Bernstein G. M., Jarvis M., 2002, AJ, 123, 583
 Blazek J., McQuinn M., Seljak U., 2011, J. Cosmol. Astropart. Phys., 5, 10
 Catelan P., Kamionkowski M., Blandford R., 2001, MNRAS, 320, L7
 Coil A. L. et al., 2011, ApJ, 741, 8
 Cool R. J. et al., 2013, ApJ, 767, 118
 Crittenden R. G., Natarajan P., Pen U.-L., Theuns T., 2001, ApJ, 559, 552
 Crittenden R. G., Natarajan P., Pen U.-L., Theuns T., 2002, ApJ, 568, 20
 Croft R., Metzler C., 2000, ApJ, 545, 561
 Cunha C. E., Lima M., Oyaizu H., Frieman J., Lin H., 2009, MNRAS, 396, 2379
 Davis M. et al., 2003, in Guhathakurta P., ed., Proc. SPIE Vol. 4834, Discoveries and Research Prospects from 6- to 10-Meter-Class Telescopes II. SPIE, Bellingham, p. 161
 Eifler T., 2011, MNRAS, 418, 536
 Eifler T., Kilbinger M., Schneider P., 2008, A&A, 482, 9
 Eifler T., Schneider P., Hartlap J., 2009, A&A, 502, 721
 Eifler T., Schneider P., Krause E., 2010, A&A, 510, 7
 Eisenstein D., Hu W., 1998, ApJ, 496, 605
 Fu L., Kilbinger M., 2010, MNRAS, 401, 1264
 Fu L. et al., 2008, A&A, 479, 9
 Heavens A., Refregier A., Heymans C., 2000, MNRAS, 319, 649
 Heymans C., Rowe B., Hoekstra H., Miller L., Erben T., Kitching T., Van Waerbeke L., 2011, MNRAS, 421, 381
 Hilbert S., Hartlap J., White S. D. M., Schneider P., 2009, A&A, 499, 31
 Hirata C., Seljak U., 2003, MNRAS, 343, 459
 Hirata C. M., Seljak U., 2004, Phys. Rev. D, 70, 63526
 Hirata C., Padmanabhan N., Seljak U., Schlegel D., Brinkmann J., 2004a, Phys. Rev. D, 70, 103501
 Hirata C. M. et al., 2004b, MNRAS, 353, 529
 Hirata C. M., Mandelbaum R., Ishak M., Seljak U., Nichol R., Pimbblet K. A., Ross N. P., Wake D., 2007, MNRAS, 381, 1197
 Hoekstra H. et al., 2006, ApJ, 647, 116
 Hopkins P., Bahcall N., Bode P., 2005, ApJ, 618, 1
 Huff E. M., Hirata C. M., Mandelbaum R., Schlegel D., Seljak U., Lupton R. H., 2011, MNRAS, 440, 1296 (Paper I)
 Huterer D., 2002, Phys. Rev. D, 65, 63001
 Ilbert O. et al., 2009, ApJ, 690, 1236
 Jain B., Seljak U., White S., 2000, ApJ, 530, 547
 Jing Y., 2002, MNRAS, 335, L89
 Joachimi B., Mandelbaum R., Abdalla F. B., Bridle S. L., 2011, A&A, 527, 26
 Jouvel S. et al., 2009, A&A, 504, 359
 Kaiser N., 2000, ApJ, 537, 555
 Kaiser E., Wilson G., Luppino G. A., 2000, preprint (astro-ph/0003338)
 Kaiser N. et al., 2010, Proc. SPIE, 7733, 12
 Kilbinger M., Schneider P., Eifler T., 2006, A&A, 457, 15
 Koekemoer A., Fruchter A., Hook R., Hack W., 2002, in Arribas S., Koekemoer A., Whitmore B., eds, Proc. Space Telesc. Sci. Inst., The 2002 HST Calibration Workshop: Hubble after the Installation of the ACS and the NICMOS Cooling System. Space Telescope Science Institute, Baltimore, MD, p. 337
 Koekemoer A. et al., 2007, ApJS, 172, 196
 Komatsu E. et al., 2011, ApJS, 192, 18
 Kovač K. et al., 2010, ApJ, 708, 505
 Krause E., Hirata C. M., 2010, A&A, 523, 28
 Kristian J., 1967, ApJ, 147, 864
 Kristian J., Sachs R. K., 1966, ApJ, 143, 379
 Larson D. et al., 2011, ApJS, 192, 16
 Laszlo I., Bean R., Kirk D., Bridle S., 2011, MNRAS, 423, 1750
 Lawrence E., Heitmann K., White M., Higdon D., Wagner C., Habib S., Williams B., 2010, ApJ, 713, 1322
 Le Fèvre O. et al., 2005, A&A, 439, 845
 Leauthaud A. et al., 2007, ApJS, 172, 219
 Lima M., Cunha C. E., Oyaizu H., Frieman J., Lin H., Sheldon E. S., 2008, MNRAS, 390, 118
 Lin H. et al., 2012, ApJ, 761, 15
 LSST Science Collaboration, 2009, preprint (arXiv:0912.0201)
 Ma Z., Bernstein G., 2008, ApJ, 682, 39
 Ma Z., Hu W., Huterer D., 2006, ApJ, 636, 21
 Madgwick D. S. et al., 2003, ApJ, 599, 997
 Mandelbaum R. et al., 2005, MNRAS, 361, 1287
 Mandelbaum R., Hirata C. M., Ishak M., Seljak U., Brinkmann J., 2006a, MNRAS, 367, 611
 Mandelbaum R., Hirata C. M., Broderick T., Seljak U., Brinkmann J., 2006b, MNRAS, 370, 1008
 Mandelbaum R. et al., 2011, MNRAS, 410, 844
 Mandelbaum R., Hirata C. M., Leauthaud A., Massey R. J., Rhodes J., 2012, MNRAS, 420, 1518
 Massey R. et al., 2007a, ApJS, 172, 239
 Massey R., Rowe B., Refregier A., Bacon D., Bergé J., 2007b, MNRAS, 380, 229
 Massey R., Stoughton C., Leauthaud A., Rhodes J., Koekemoer A., Ellis R., Shaghoulouian E., 2010, MNRAS, 401, 371

- Miller L. et al., 2013, MNRAS, 429, 2858
Miyazaki S. et al., 2006, Proc. SPIE, 6269, 9
Moster B., Somerville R., Newman J., Rix H.-W., 2011, ApJ, 731, 113
Nakajima R., Mandelbaum R., Seljak U., Cohn J. D., Reyes R., Cool R., 2011, MNRAS, 420, 3240
Okumura T., Jing Y. P., Li C., 2009, ApJ, 694, 214
Perlmutter S. et al., 1999, ApJ, 517, 565
Refregier A., 2003, MNRAS, 338, 35
Refregier A., Amara A., Kitching T. D., Rassat A., 2011, A&A, 528, 33
Reyes R., Mandelbaum R., Gunn J. E., Nakajima R., Seljak U., Hirata C. M., 2012, MNRAS, 425, 2610
Rhodes J. et al., 2007, ApJS, 172, 203
Riess A. G. et al., 1998, AJ, 116, 1009
Schmidt F., Rozo E., Dodelson S., Hui L., Sheldon E., 2009, ApJ, 702, 593
Schneider P., Kilbinger M., 2007, A&A, 462, 841
Schneider P., van Waerbeke L., Mellier Y., 2002, A&A, 389, 729
Schneider P., Eifler T., Krause E., 2010, A&A, 520, 116
Schrabback T. et al., 2010, A&A, 516, 63
Scoville N. et al., 2007a, ApJS, 172, 1
Scoville N. et al., 2007b, ApJS, 172, 38
Semboloni E. et al., 2006, A&A, 452, 51
Sheldon E., Cunha C., Mandelbaum R., Brinkmann J., Weaver B., 2011, ApJS, 201, 32
Smith R. et al., 2003, MNRAS, 341, 1311
The Dark Energy Survey Collaboration, 2005, preprint (astro-ph/05010346)
van Waerbeke L. et al., 2000, A&A, 358, 30
van Waerbeke L., White M., Hoekstra H., Heymans C., 2006, *Astropart. Phys.*, 26, 91
Wittman D. M., Tyson J. A., Kirkman D., Dell'Antonio I., Bernstein G., 2003, MNRAS, 341, 1311
Zhang J., Komatsu E., 2011, MNRAS, 414, 1047

APPENDIX A: THE DATA VECTOR AND COVARIANCE MATRIX

Here we reprint the data vector (Table A1) and covariance matrix (Table A2) used in this measurement. The code used to project the correlation function on to the COSEBI basis functions is available from the authors upon request.

Table A1. Our data vector. The first five elements are the COSEBI mode amplitudes; the final is the correlation function averaged in the range $29.2296 \leq \theta \leq 44.9730$.

4.897 97E-10
1.283 35E-09
1.251 36E-09
1.456 16E-09
8.923 33E-10
1.464 57E-05

Table A2. The covariance matrix for the data vector shown in Table A1.

Data vector index	Data vector index	Covariance
0	0	3.371 61E-20
0	1	4.676 37E-20
0	2	4.004 84E-20
0	3	2.499 16E-20
0	4	9.842 57E-21
0	5	3.017 70E-17
1	1	1.063 83E-19
1	2	1.192 26E-19
1	3	8.395 08E-20
1	4	3.865 19E-20
1	5	1.823 44E-16
2	2	1.999 23E-19
2	3	1.874 69E-19
2	4	1.121 96E-19
2	5	5.077 90E-16
3	3	2.565 68E-19
3	4	2.133 63E-19
3	5	8.021 18E-16
4	4	2.677 74E-19
4	5	5.677 97E-16
5	5	3.681 12E-11

This paper has been typeset from a $\text{\TeX}/\text{\LaTeX}$ file prepared by the author.